

State-of-the-art models for the phase diagram of carbon and diamond nucleation

L. M. Ghiringhelli^{1*}, C. Valeriani^{2†}, J. H. Los³, E. J. Meijer¹,
A. Fasolino^{1,3}, and D. Frenkel^{1,2‡}

¹ van 't Hoff Institute for Molecular Sciences, Universiteit van Amsterdam,
Nieuwe Achtergracht 166, 1018 WV Amsterdam, The Netherlands.

² FOM Institute for Atomic and Molecular Physics,
Kruislaan 407, 1098 SJ Amsterdam, The Netherlands.

³ Institute for Molecules and Materials, Radboud University Nijmegen
Heyendaalseweg 135, 6525 AJ Nijmegen, The Netherlands

October 23, 2018

Abstract

We review recent developments in the modelling of the phase diagram and the kinetics of crystallization of carbon. In particular, we show that a particular class of bond-order potentials (the so-called LCBOP models) account well for many of the known structural and thermodynamic properties of carbon at high pressures and temperatures. We discuss the LCBOP models in some detail. In addition, we briefly review the “history” of experimental and theoretical studies of the phase behaviour of carbon. Using a well-tested version of the LCBOP model (viz. LCBOP⁺) we address some of the more controversial hypotheses concerning the phase behaviour of carbon, in particular: the suggestion that liquid carbon can exist in two phases separated by a first-order phase transition and the conjecture that diamonds could have formed by homogeneous nucleation in Uranus and Neptune.

1 Introduction

Carbon exhibits a rich variety of solid structures: Some are thermodynamically stable, most are not. To be specific: solid carbon can be found in the two well-

known crystalline phases, diamond and graphite, and in amorphous states, such as glassy carbon and carbon black. Furthermore, the existence of additional metastable solid phases at relatively low pressure, the so-called carbynes, is still hotly debated [1, 2]). In addition to the bulk phases, there are the more recently discovered fullerenes, C₆₀ and C₇₀ [3], nanotubes [4], and graphene [5].

The reason why a simple element such as carbon can manifest itself in so many different forms is related to its unusual chemical properties: carbon exhibits three different possibilities for covalent bond formation: *sp*₃ hybridization appears in diamond, *sp*₂ hybridization is found in graphite, graphene, nanotubes, and fullerenes, whilst in carbynes, C should exhibit *sp* hybridization. Because of their high cohesive energies and concomitant high activation energies that must be overcome in structural phase transformations, carbon polymorphs often exist in metastable form well inside pressure-temperature regions where another solid form is thermodynamically stable. For example, it is well known that diamonds survive at normal P-T conditions, where graphite is the thermodynamically stable phase. Conversely, graphite tends to persist at very high pressures, deep into the diamond stability region of the phase diagram.

It is also interesting that, at zero pressure and temperature, graphite and diamond have a very similar (and quite large) binding energy *per atom*, i.e. 7.37 eV (graphite) vs 7.35 eV (diamond). This fact might suggest (and it has indeed been suggested) that also in

*Current address: Max-Planck-Institute for Polymer Research, Ackermannweg 10, 55128 Mainz, Germany

†Current address: School of Physics, James Clerk Maxwell Building, King's Buildings, University of Edinburgh, Mayfield Road, EH9 3JZ, Edinburgh, UK

‡Current address: Dept. of Chemistry, University of Cambridge, Lensfield Road, Cambridge CB2 1EW, UK

disordered phases like the liquid, the two local structures – graphite-like and diamond-like – could compete. In fact, as we discuss below, the possibility of the existence of two distinct and partially immiscible liquid phases of carbon has been a subject of much debate.

In a liquid–liquid phase transition (LLPT), a liquid substance displays an abrupt change in some local or global property within a narrow band of pressures and temperatures. Local properties that may change in a LLPT are the local coordination or hybridization, typical global properties that are affected are the density or the resistivity. LLPT’s in dense, atomic liquids are typically difficult to probe experimentally: the candidate transitions often occur at extreme pressures and/or temperatures or appear in metastable regions of the phase diagram (and may be hidden by competing solidification). Evidence for LLPT’s have been found for a number of atomic systems, such as Cs [6], As [7], Bi [8], Ge [9], Hg [10], S [11], Sb [12], Se [13], Si [14, 15], Sn [16], H₂ [17], I₂ [18], N₂[19, 20]. The best established experimental example of a LLPT in an atomic liquid is the case of phosphorus. A transition between a fluid of tetrahedral P_4 molecules and a network forming (and metallic) liquid was predicted on theoretical grounds [21, 22], and subsequently verified experimentally [23, 24]. The LLPT in phosphorus has been analysed in several numerical studies [25, 26, 27, 28]. Many other network-forming liquids are also expected to exhibit LLPT’s: first and foremost water [29, 30], but also SiO₂ [31] and GeO₂ [32]. Although considerable progress has been made in the theoretical description of LLPT’s [33, 34, 35, 36, 37, 38], a unified theoretical picture is still lacking.

In this review we discuss the phase diagram of solid and liquid carbon at high pressures and temperatures on the basis of the results of numerical simulations; both quantum and classical. We present evidence that the presence of graphite-like and diamond-like local structures in the liquid does not give rise to liquid-liquid demixing but that the predominant local structure in the liquid varies strongly with pressure. The fact that the liquid is locally either graphite-like or diamond-like has dramatic consequences for the nucleation of the diamond phase, a finding that may have some consequences for our understanding of carbon-rich planets or stars. Wherever possible, we discuss our own results in the context of the relevant literature about the carbon phase diagram, about a possible LLPT in this system and about the possibility of diamond formation in planetary interiors.

In section 2 we give an overview of the bond-order potential (“LCBOP”) that was used to compute both the equilibrium phase diagram of carbon and the path-

way for diamond nucleation in liquid carbon. We also discuss in some detail the different variants of the LCBOP potential [39, 40] and explain the rationale behind the choice of the present LCBOP potential.

In section 3 we briefly summarize some of the earlier ideas about the phase diagram of carbon (in particular, about the crystalline phases and the liquid). We pay special attention to the slope of the diamond melting curve and the (possible) heating-rate dependence of the graphite melting curve.

In section 3.2 we report our results concerning the phase diagram, in the context of recent first-principle simulations and experiments.

In section 4.1 we review the arguments that have been put forward to support the idea that liquid carbon can undergo a LLPT. We argue that, to the extent that we can trust the present models of liquid carbon, a LLPT in carbon is not be expected.

In section 5 we discuss our numerical results concerning the (homogeneous) nucleation of diamond from the bulk liquid. In particular, we discuss in some detail the numerical approach that was used in Ref. [41]. In addition, we focus on the structural analysis of the small solid clusters in the liquid and we discuss the implications of our findings for the formation of diamonds in carbon-rich star systems and the interior of giant planets.

2 The LCBOP-family

Whilst the crystalline phases of carbon can be simulated by traditional force fields that do not allow coordination changes, a study of the liquid phase and, a fortiori, of phase transformations between phases with different local coordination, requires a potential that can describe carbon in different coordination states. The LCBOP potential was designed with this objective in mind. LCBOP stands for “Long range Carbon Bond Order Potential”, and represents a bond-order potential for pure carbon that includes long-range (LR) dispersive and repulsive interactions [39] from the outset. We stress that LCBOP is not based on an existing short-range (SR) bond-order potential to which LR interactions have been added a posteriori, although such an approach has been proposed in the literature [42, 43, 44]. The latter approach requires a rather special procedure to avoid interference with the SR potential and suffers from a loss of accuracy. In the LCBOP these problems are circumvented in a natural way.

We note that the term “long range” may be confusing in this case, as the cut-off of the LR potential in LCBOP is only 6 Å. Usually, the term “long range” is

only used for interactions with a much longer range, such as Coulomb interactions. Here we use it as a synonym for "non-bonded", referring to a range much larger than the typical distances between chemically bonded atoms.

After the introduction of LCBOP in Ref. [39], a number of significant modifications have been introduced in order to improve its description of all carbon phases, including liquid carbon. To facilitate the distinction between the different LCBOP potentials, the various versions have been named LCBOP, LCBOP⁺ and LCBOPII. LCBOP, introduced as LCBOP in Ref. [39], does not include torsion interactions. As torsion interactions were shown to play an important role in liquid carbon [45], we introduced a refinement of LCBOP, called LCBOP⁺, when we performed our first study of liquid carbon [46]. LCBOP⁺, includes, among other changes, conjugation dependent torsional interactions. Clearly, describing the liquid phase requires a robust form of the potential in order to deal with configurations that are quite unlike the regular topologies in crystal lattices. LCBOPII addresses this problem: it includes several important improvements over LCBOP⁺. An important innovation in LCBOPII is the addition of so-called middle range (MR) interactions, introduced to bridge the gap between the extent of the tail of the covalent interactions as found in *ab-initio* calculations, (up to 4.5 Å in certain cases) and the rather short cut-off of only 2.2 Å in LCBOP⁺ for these interactions.

In the remainder of this section we give a brief step-by-step description of the transition from bond-order potentials (BOPs) to LCBOP⁺. All the results presented in later sections, concerning the phase diagram, the liquid structure, and the nucleation issues are obtained with this version of the potential. In Appendix A we discuss the LCBOPII potential, with a short account of results obtained with this refined version of the potential. We aim at giving the flavour of the potentials in a mainly descriptive way with graphical illustrations, minimizing mathematical formulation.

2.1 Bond-order potentials

A bond-order potential (BOP) is a reactive potential, i.e. able to deal with variable coordination. It provides a quantitative description of the simple idea that the bonds of an atom with many neighbours are weaker than those of an atom with few neighbours, as the cohesive ability of the available electrons has to be shared among the neighbours. For carbon, each atom delivers four valence electrons. If these four electrons have to make the six bonds in a simple cubic lattice, then it is

evident that each of these bonds is weaker than a bond in the diamond or graphite lattice with coordinations 4 and 3 respectively. On the other hand, the number of bonds is larger for the simple cubic lattice. So there is a balance to be made, which in the case of carbon has the result that graphite is the most stable phase at ambient pressure.

A thorough analysis of these bonding properties, based on a quantum mechanical description, has been given by Anderson [47, 48, 49] and Abell [50]. In their description, that forms the basis of the tight binding models, the electronic wave function is approximated as a sum of localized atomic orbitals. Abell showed that for a regular lattice, i.e. with an identical environment for each atom, and within the assumption that the overlap integral for orbitals on different atoms is non-vanishing only for nearest neighbours, the binding energy per atom is given by:

$$E_b = \frac{1}{2}Z(qV_R(r) + bV_A(r)) \quad (1)$$

where Z is the number of nearest neighbours, q is the number of valence electrons per atom, $V_R(r)$ is a two-body potential describing the core repulsion, $V_A(r)$ is a two-body attractive potential, and b is the so-called bond order, a many-body term dependent on the local environment of the atoms. Abell also showed that the coordination dependence of b is fairly well approximated by:

$$b = b(q, Z) = \alpha(q)Z^{-1/2} \quad (2)$$

with $\alpha(q)$ a function of q , specified in Ref. [50]. Assuming exponential functions $V_R(r) = A \exp(-\theta r)$ and $V_A(r) = -B \exp(-\lambda r)$, with A , B , λ , and θ fitting parameters, as a reasonable approximation for overlapping atomic orbitals from atoms at distance r , and defining $S = \theta/\lambda$, some algebra leads to a total binding energy given by:

$$\begin{aligned} E_b &= B\alpha(q) \frac{S-1}{2S} \left(\frac{B\alpha(q)}{qAS} \right)^{\frac{1}{S-1}} Z^{\frac{S-2}{2(S-1)}} \\ &= CZ^{\frac{S-2}{2(S-1)}} \end{aligned} \quad (3)$$

and an equilibrium nearest neighbour distance given by:

$$r_{eq} = \frac{1}{\theta - \lambda} \ln \left(\frac{qAS\sqrt{Z}}{B\alpha(q)} \right) = \frac{1}{2(\theta - \lambda)} \ln Z + C' \quad (4)$$

where C and C' are constants. Eq. 3 implies that for $S > 2$ high coordination structures (close packing) are favoured (metals), whereas for $S < 2$ the dimer will

be the most stable structure (extreme case of covalent bonding). As, in general, the repulsion falls off (much) faster than the attraction, i.e. $\theta > \lambda$ ($S > 1$), Eq. 4 implies that r_{eq} is monotonically increasing with coordination. Combining Eqs. 3 and 4 yields a simple relation between E_b and r_{eq} , namely $E_b \propto \exp(\theta - 2\lambda)r_{eq}$.

In principle BOPs are based on the above bonding ideas. However, the transferability to different types of structures and materials has been greatly enhanced by a quite reasonable extension in the functional form of the bond order b_{ij} for a bond ij according to a BOP in the style of Tersoff [51] and Brenner [52] reads:

$$b_{ij} = \alpha \left(1 + \sum_{k \neq i,j} G(\theta_{ijk}) \right)^\epsilon \quad (5)$$

where the sum runs over the nearest neighbours other than j of atom i , $G(\theta_{ijk})$ is an adjustable function of the bond angles θ_{ijk} and ϵ is a negative exponent but not necessarily $-1/2$. Taking a constant $G(\theta_{ijk}) = 1$ and $\epsilon = -1/2$ yields $b = \alpha Z^{-1/2}$, i.e. one recovers the functional form Abell found for b (Eq. 2). This form includes the effect of bond angles in a natural way, and has the ability to fit a large set of data quite well, explaining the success of BOPs.

2.2 LCBOP

The main innovative feature of LCBOP [39] concerns the treatment of the LR van der Waals interactions. One of the challenges here is to add LR interactions which describe not only the interlayer graphitic binding but also the rather strong π -bond repulsion in graphite for decreasing interlayer distance without paying a price in the accuracy of the covalent binding properties. A correct description of these interactions requires a LR potential, $V^{lr}(r)$ that is repulsive in the distance range corresponding to the second nearest neighbours (in diamond and graphite). In the LCBOP-family, to get the right equilibrium lattice parameter, this extra repulsion has been compensated by a somewhat stronger attractive part of the covalent interaction, achieved by an appropriate parametrisation of the SR potential. This is schematically illustrated in Fig. 1.

Another feature of LCBOP is that it contains a reasonable, physically motivated interpolation scheme for the conjugation term to account for a mixed saturated and unsaturated environment. In this approach each atom supplies a number of electrons to each of its bonds with neighbouring atoms according to a certain distribution rule, the total sum being equal to the valence

value 4 of carbon. The character of a certain bond ij , and its conjugation number N_{ij}^{conj} , a number between 0 and 1 quantifying effects beyond nearest neighbours, is determined by the sum of the electrons supplied by atom i and atom j . The interpolation model is further illustrated in Fig. 2.

2.3 LCBOP⁺

The potential LCBOP⁺ is given by LCBOP supplemented with torsion interactions and a correction of the angle dependent part of the bond order for configurations involving low coordinations and small angles. Similar modifications were also included in the REBO potential [53], although the torsion term contains a significant difference. For LCBOP⁺, following the results of ab-initio calculations, the shape of the torsion energy curve as a function of the torsion angle depends on conjugation, whereas for the REBO potential the curves for a double and a graphitic bond are equally shaped but scaled (see top panel of Fig. 20). Details on LCBOP⁺ are given in the appendix A of Ref. [54] and in Ref. [55].

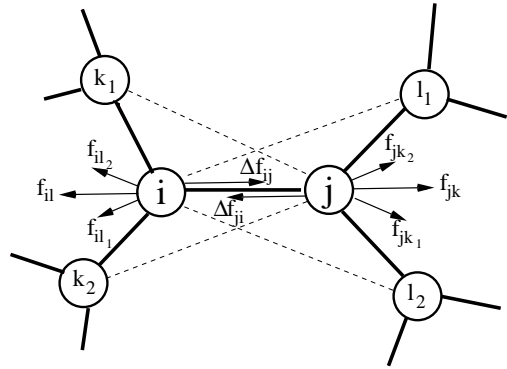


Figure 1: Schematic representation of the LCBOP approach to the inclusion of LR interactions. To preserve the right equilibrium bond distance for a given bond ij , the repulsion of atom i due to the added LR interactions with the atoms l_1 and l_2 (represented by the force $\mathbf{f}_{il} = \mathbf{f}_{il_1} + \mathbf{f}_{il_2}$) is compensated by a stronger attractive part in the SR interaction between i and j , represented by the extra force $\Delta \mathbf{f}_{ij}$. The same holds for atom j . For convenience, here only the main, repulsive LR interactions are drawn, whereas in reality this compensation is for the sum of all LR interactions.

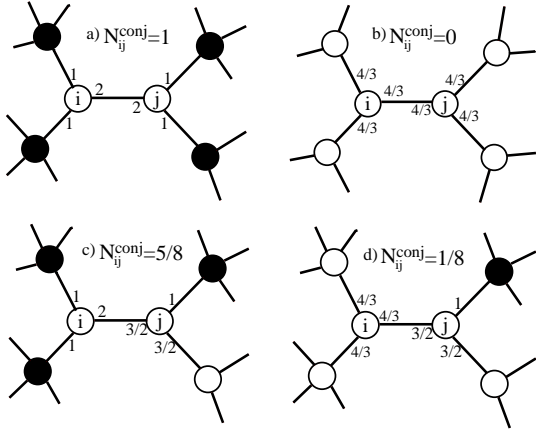


Figure 2: Schematic presentation of the interpolation approach in the determination of N_{ij}^{conj} for mixed coordination situations (c and d). Black atoms are saturated atoms, white atoms are unsaturated. The numbers near the atoms i and j indicate the distribution of electrons among their bonds. Each single bond, i.e. a bond with a saturated neighbour, takes 1 electron. The remainder of the electrons (in total 4) are equally shared among the bonds with unsaturated atoms. A linear dependence of N_{ij}^{conj} on the total number of electrons involved in the bond ij with $0 \leq N_{ij}^{conj} \leq 1$ as an additional constraint leads to the given values for N_{ij}^{conj} .

3 The phase diagram of carbon at very high pressures and temperatures

In this section we give a review of experimental and theoretical works aimed at determining the phase behaviour of carbon at high temperatures and pressure. We follow a “historical” approach, starting from the beginning of the twentieth century, up to the most recent results coming from experiments and computer simulations. A historical approach may give a better understanding why certain issues have been, and in some case still are, controversial. After setting the stage (with a particular attention to the ideas about the sign of the slope of the diamond melting curve and the long debated issue of the position and nature of the graphite melting curve), we focus on the topic of the LLPT for carbon.

3.1 The history of carbon phase diagram

One of the earliest phase diagrams of carbon appeared at the beginning of the twentieth century, and is due to H. Bakhuis Roozeboom [56], who estimated the phase behavior of carbon on the basis of thermodynamic arguments. Of the two solid phases, diamond was recognized to have a slightly greater vapor pressure at a given temperature. The temperature of the graphite/liquid/vapor triple was believed to be around 3000 K. In 1909 Tamman [57] postulated the existence of a region where graphite and diamond are in pseudo-equilibrium. The existence of this pseudo-equilibrium region was at the basis of the method of synthesizing diamond starting from carbon saturated solutions of molten iron, silver, or silicates. In 1938, Rossini and Jessup [58] of the U.S. Bureau of Standards used accurate thermodynamic data to estimate that at 0 K the lowest pressure at which diamond would be stable against graphite is around 1.3 GPa, and around 2 GPa at 500 K. In 1939, the Russian scientist Leipunskii [59] published a review of the problem of diamond synthesis. On the basis of thermodynamic data, he suggested that the melting curve of graphite might be at about 4000 K, with possibly some increase with pressure. This value for the melting of graphite was rather well verified the same year by Basset [60], who established the graphite/liquid/vapor triple point to be at about 11 MPa and 4000 K. In that same publication, Basset reported on a rather pressure independent melting temperature of graphite at ~ 4000 K, from atmospheric pressure up to 0.1 GPa. In 1947 Bridgman [61] addressed the problem of extrapolating the graphite/diamond coexistence curve beyond the region where it can be estimated from known physical properties (4 GPa/1200 K). He concluded that there was a possibility that at higher temperatures the rate of increase of P with T along the curve would decrease. This hypothesis was later supported by Liljebblad [62] in 1955, while Berman and Simon [63] in the same year came to the conclusion that the best extrapolation would be a straight line. Experiments that could decide this issue were started by Bundy and coworkers in 1954, when they accomplished diamond synthesis by activating the graphite-to-diamond reaction with the use of different solvent-catalyst metals. The relevant experimental data were published only much later [64, 65], and are compatible with the Berman-Simon straight line extrapolation.

Bundy and his group made also extensive experiments on graphite melting at pressures much higher than the graphite/liquid/vapor triple point. The determination

of the graphite melting curve is an experimental challenge for several reasons. First of all, to reach pressures as high as 10 GPa, the sample must be in direct contact with a solid container and, because the melting temperature are so high, this container must be made of a material that is as refractory and inert as possible (Bundy chose boron nitride, pyrophyllite, MgO and diamond powder). In addition, both the heating of the sample and the observations of the high-pressure/high-temperature phase must be carried out very rapidly, before the wall material can melt or react with the carbon sample. The experiments were performed by discharging an electrical capacitor through the sample (this procedure is known as flash heating), and by monitoring the current through, and the voltage across it by means of a two-beam oscilloscope. The discharge circuit was designed to have energy insertion in the sample within a few milliseconds. The interpretation of such experiments, is rather sensitive to the assumed pressure and temperature dependence of the material under study and on the assumption that the pressure of the graphite specimen during rapid heating is the same as in a quasi-static process. With these assumptions, Bundy's experiments gave a graphite melting curve as shown in Fig. 3. A maximum melting temperature of about 4600 K was detected in the region of 6 GPa to 7 GPa. The presence of a region with a negative dT/dP along the melting curve indicates that, at those pressures, the density of the liquid at the melting temperature is greater than that of the solid.

Interrupting for a moment the historical order of events, we note that, throughout the past century, different experiments located the graphite melting curve at rather different temperatures [66, 60, 67, 68, 65, 69, 70, 71, 72, 73, 74, 75]. At low pressure, the melting temperature (T_m) was found at values ranging from ~ 3800 to ~ 5000 K. Asinovskii *et al.* [76] pointed out the non negligible dependence of graphite T_m on the heating rate of the sample. Specifically, heating times of the order of 10^{-5} s [70, 72] yielded estimates of $T_m \sim 4800 - 5000$ K; heating times of the order of 10^{-3} s [71, 74] suggested $T_m \sim 4500 - 4600$ K; finally experiments with heating times of the order of one second [60, 69] were consistent with the assumption that $T_m \sim 3800 - 4000$ K. In ref [76], after a thorough discussion of the experimental methods, the authors recommended that only data coming from experiments with heating time of the order of seconds or more should be accepted. This implied that most of the available data on graphite melting had to be reconsidered and that the question of the position and the shape of the melting curve is still open. On the basis of a series of laser induced slow heating experiments [76] (i.e. heat-

ing times of the order of one second), Asinovskii *et al.* proposed the triple point vapor/liquid/graphite at ~ 4000 K and 0.1 MPa (i.e. atmospheric pressure), in clear contradiction to the commonly accepted values [73] of ~ 5000 K and 10 MPa. The next year the same authors [77] published results concerning the position of the graphite melting curve. With ohmic heating of graphite samples at heating rates of about 100 K/minute, they found $T_m = 3700$ K at 0.25 MPa (typically, samples melted after one hour of steady heating).

Coming back to Bundy's work, during the experiments on graphite melting Bundy and his group also investigated the graphitization of diamond by flash-heating under pressure. Small diamond crystals were embedded in the graphite sample, pressurized and then flash-heated. Experiments indicated that there is a sharp temperature threshold at which the diamond crystals completely graphitized. This threshold is a few hundreds degrees lower than the graphite melting curve. Attempts to obtain direct (i.e. without resorting to a catalyst material) conversion of graphite into diamond by the application of high pressure date back to the beginning of the twentieth century. Success came only in 1961, when De Carli and Jamieson [78] reported the formation and retrieval of very small black diamonds when samples of low-density polycrystalline graphite were shock compressed to pressures of about 30 GPa. Later in 1961 Alder and Christian [79] reported results on the shock compression of graphite that were in substantial agreement with those of De Carli and Jamieson.

Bundy [80] achieved direct conversion of graphite into diamond by flash-heating graphite sample in a static pressure apparatus, at pressures above the graphite/diamond/liquid triple point. The threshold temperature of the transformation was found several hundred degrees below the melting temperature of the graphite, and decreasing at higher pressures. The phase transition was revealed by a sharp drop in the electrical conductivity of the samples (that were retrieved as pieces of finely polycrystalline black diamond).

By linking his own results with earlier experimental and theoretical findings, Bundy [80] proposed in February 1963 a phase diagram of carbon at high pressures that is illustrated in Fig. 3. The diamond melting curve was believed to have negative slope by analogy with the other Group IV elements [81, 82]), and on the basis of evidence collected during the experiments of Alder and Christian [79].

In 1973 Van Vechten [83] predicted the phase diagram of carbon by rescaling the behavior of other Group IV

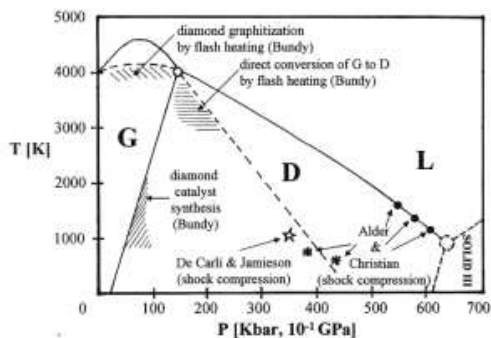


Figure 3: The phase diagram of carbon at high pressures proposed by Bundy in 1963 [80].

elements that are experimentally more accessible, using the electronegativity as a scale parameter. In 1979 Grover [84] calculated a phase diagram by using a phenomenological equation of state for the description of various solid and liquid phases of carbon. He used physically motivated approximations for the free energies of the various phases, with parameters adjusted to match the available data on the equations of state. He concluded that, at all pressures, diamond transforms, before melting, into a solid metallic phase.

On the basis of experimental evidence [85], in 1978 Whittaker [1] proposed the existence of a novel crystalline phase for elemental carbon, called “carbyne”. The stability region of carbyne is sketched in Fig. 4) and the structure of this phase (though expected in different allotropes) is generally that of a chains of alternated single and triple bonds, i.e. $(-C\equiv C-)_n$, arranged in a hexagonal array bundled by dispersion interactions. The existence of a carbyne form was later questioned by Smith and Buseck [2], who claimed that all the experimental evidence could also be accounted for by the presence of sheet silicates. This dispute continued to this day: the experimental evidence for the existence of carbyne is still being debated.

In recent years, the experimental effort has focused on the collection of reliable data at even higher pressures, and on the investigation of the properties of the different phases of carbon at high temperatures and pressures. This challenging task has been faced both with experiments and theory. On the experimental side, the development of the diamond-anvil cell [6] for high pressure physics has made it crucial to know the range of stability of diamond under extreme conditions. The availability of high-energy pulsed laser sources led to new tools for heating up samples at very high temperatures (above the graphite melting curve) [86]. These

techniques were immediately applied to the determination of the properties of liquid carbon (i.e. whether it is a conducting metallic liquid or an insulator). Unfortunately, due to the difficulties in interpreting the results of these experiments, the nature of the liquid state of carbon is still not characterized experimentally.

On the theoretical side, the appearance of ever more powerful computers made it possible to use electronic density-functional (DF) theory [87, 88] to predict the properties of materials under extreme conditions. In 1983 Yin and Cohen [89] studied the total energy versus volume and the free energies versus pressure for the six possible lattices of carbon (fcc, bcc, hcp, simple cubic, β -tin, diamond). The study was carried out by using ab initio pseudopotential theory (this permits the investigation of the properties of the atomic system at 0 K). Yin and Cohen found that the calculated zero-pressure volume for diamond is either close to or even smaller than those of the other five phases. This is different from what is observed for the other group IV elements, Si and Ge, and defies the common notion that diamond is an open structure and should have higher specific volume than the close packed solid structures. The relatively dense packing of diamond would inhibit the phase transformations at high hydrostatic pressures that are observed for heavier group IV elements. In addition, it suggested a revision of the other common notion that the diamond melting curve should have negative slope, something that is to be expected when a liquid is denser than the co-existing solid. Yin and Cohen also found that, at a pressure around 2300 GPa, diamond converts to a simple cubic (sc) phase. This work was later extended [90, 91, 92] to consider also complex tetrahedral structures. It was found that a distorted diamond structure called BC-8 was stable versus diamonds at pressures above 1000 GPa (see Fig. 4).

In 1984 Shaner and coworkers [93] shock compressed graphite and measured the sound velocity in the material at shock pressures ranging from 80 to 140 GPa, and corresponding shock temperatures ranging from 1500 to 5500 K. They measured velocities close to those of an elastic longitudinal wave in solid diamond. These velocities are much higher than those of a bulk wave in a carbon melt. Since no melt was detected at pressures and temperatures well above the graphite/diamond/liquid triple point, the diamond melting curve should, according to these results, have a positive slope. In 1990 Togaya [94] reported experiments in which specimens of boron-doped semiconducting diamond were melted by flash-heating at pressures between 6 and 18 GPa: these experiments provided clear indications that the melting tempera-

ture of diamond increases with pressure.

In the same year ab-initio molecular dynamics (MD) studies [95] clearly showed that, upon melting diamond at constant density, the pressure of the system increases. These results imply that, at the densities studied, the slope of the melting curve of diamond is positive. The shape of the diamond melting curve has interesting consequences for the theory of planetary interiors. Given our present knowledge of the phase diagram of carbon and the existing estimates for the temperatures and pressures in the interior of the outer planets Neptune and Uranus, as well as in the Earth mantle, one might conclude that in a large fraction of these planetary interiors the conditions are such that diamond should be the stable phase of carbon [96]; diamonds could then be expected to occur wherever the carbon concentration is sufficiently high. In section 5 we show that, when only homogeneous nucleation is considered, our modelling predict that the driving force for diamond nucleation is missing in giant planet interiors. In 1996 Grumbach and Martin [97] made a systematic investigation of the solid and liquid phases of carbon over a wide range of pressures and temperatures by using ab initio MD. These authors studied the melting of the simple cubic and BC-8 solid phases, and investigated structural changes in the liquid in the range 400-1000 GPa. They observed that the coordination of the liquid changes continuously from about four-fold to about six-fold over this pressure range.

In 2004, Bradley *et al.* [98] reported experiments on laser-induced shock compression of diamond up to 3000 GPa. Through optical reflectivity measurements, they found for the first time direct evidences of diamond melting, at an estimated pressure of $P = 1000 \pm 200$ GPa, and temperature $T = 12000 \pm 4000$ K.

Fig. 4 summarizes the information about phase diagram of carbon at the time when the present research was started.

3.2 Carbon phase diagram according to LCBOP

Methods We performed Monte Carlo simulations on the LCBOP⁺ model of carbon [39, 46] to estimate the properties of the liquid, graphite, and diamond phases of carbon. Coexistence curves were determined by locating points in the $P-T$ diagram with equal chemical potential for the two phase involved. For this purpose, we first determined the chemical potential for the liquid, graphite, and diamond at an initial state point ($P = 10$ GPa, $T = 4000$ K). This state point is near the estimated triple point[99]. Subsequently, the liquid-graphite, liquid-diamond, and graphite-diamond coex-

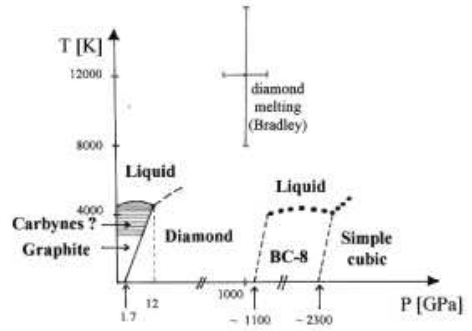


Figure 4: In 2004, a schematic representation of the phase diagram of carbon at high pressures would have looked more or less as indicated in this figure. Full curves correspond to phase boundaries for which thermodynamic data are available. More recent developments are discussed in the next section.

istence pressures at $T = 4000$ K were located. In turn, these coexistence points served as the starting point for the determination of the graphite melting line, the diamond melting line, and the graphite-diamond coexistence curve, obtained by integrating the Clausius-Clapeyron equation (a procedure also known as Gibbs-Duhem integration) [100]: $\frac{dT}{dP} = \frac{T\Delta v}{\Delta h}$ where Δv is the difference in specific volume, and Δh the difference in molar enthalpy between the two phases.

We proceeded by first determining the Helmholtz free energy at a given density and temperature by thermodynamic integration and subsequently calculating the chemical potential using the procedure described in Ref. [101]. Coexistence at a given T is found at the P where the different μ cross.

For all phases, the Helmholtz free energy F^{\boxtimes} of the initial state point ($P = 10$ GPa, $T = 4000$ K) was determined by transforming the system into a reference system of known free energy F^{ref} . The transformation was imposed by changing the interaction potential: $U_{\lambda} = (1 - \lambda)U^{\boxtimes} + \lambda U^{\text{ref}}$. Here, U^{\boxtimes} and U^{ref} denote the potential energy function of the LCBOP⁺ and the reference system, respectively. The transformation is controlled by varying the parameter λ continuously from 0 to 1. The free-energy change upon the transformation was determined by thermodynamic integration:

$$\begin{aligned} F^{\boxtimes} &= F^{\text{ref}} + \Delta F^{\text{ref} \rightarrow \boxtimes} = \\ &= F^{\text{ref}} + \int_{\lambda=0}^{\lambda=1} d\lambda \left\langle \frac{\partial U_{\lambda}}{\partial \lambda} \right\rangle_{\lambda} = \\ &= F^{\text{ref}} + \int_0^1 d\lambda \langle U^{\text{ref}} - U^{\boxtimes} \rangle_{\lambda} \end{aligned} \quad (6)$$

The symbol $\langle \dots \rangle_\lambda$ denotes the ensemble average with the potential U_λ .

As reference system for the liquid we chose the well-characterized Lennard-Jones (12-6) system, whilst the reference system for both diamond and graphite was the Einstein crystal. General guidelines for these kind of calculations are given in [102, 101], while a full description of the strategy adopted for the present systems is given in [55]. The ensemble averages needed for the thermodynamic integration were determined from Monte Carlo (MC) simulations of a 216-particle system in a periodically replicated simulation box. For simulations of the graphite phase, the atoms were placed in a periodic rectangular box with an initial edge-size ratio of about 1 : 1.5 : 1.7. For the liquid phase and diamond a periodic cubic box was used.

From the Helmholtz free energy to the chemical potential The chemical potential μ along the 4000 K isotherm was obtained by integrating from the initial state point a fit, $P(\rho) = a + b\rho + c\rho^2$, through simulated (P, T) state points along the 4000 K isotherm. Here, ρ is the number density, and a , b , and c are fit parameters. This yields for the chemical potential [101]:

$$\beta\mu(\rho) = \frac{\beta F^\boxtimes}{N} + \beta \left(\frac{a}{\rho^\boxtimes} + b \ln \frac{\rho}{\rho^\boxtimes} + b + c(2\rho - \rho^\boxtimes) \right) \quad (7)$$

Here, ρ^\boxtimes denotes the number density at the initial state point, N the number of particles, and $\beta = 1/k_B T$, with k_B the Boltzmann constant.

Calculated coexistence curves The equilibrium densities $\rho^\boxtimes/(10^3 \text{ kg/m}^3)$ at the initial state point ($P = 10 \text{ GPa}$, $T = 4000 \text{ K}$) were 3.425 for diamond, 2.597 for graphite, and 2.421 for the liquid. Three configurations at the equilibrium volume were then chosen as starting state point for the free energy calculation.

	a [GPa]	b [GPa nm ³]	c [GPa nm ⁶]
Liquid	89.972	-1.9654	0.011 092
Diamond	74.809	-3.6307	0.019 102
Graphite	108.29	-2.2707	0.011 925

Table 1: Parameters for the polynomial fitting of the 4000 K isotherms of the three phases, according to: $P(\rho) = a + b\rho + c\rho^2$.

The integrals related to the reference system transformation (Eq. 6) were evaluated using a 10-point Gauss-Legendre integration scheme. Fig. 5 shows the integrand $\langle U^{\text{ref}} - U^{\text{LCBOPI}^+} \rangle_\lambda$ versus λ . The smooth behaviour of the curves indicates that there are no spurious phase transitions upon the transformation to the

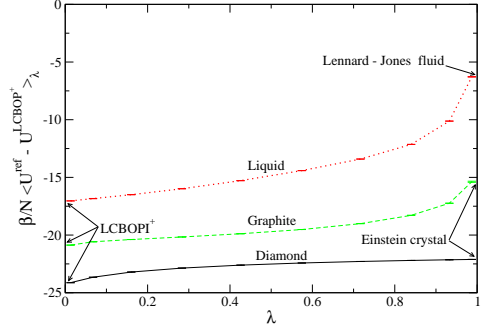


Figure 5: Plots of the quantity $\beta/N \langle U^{\text{ref}} - U^{\text{LCBOPI}^+} \rangle_\lambda$ (see Eq. 6) as a function of the coupling parameter λ for the liquid, graphite, and diamond. On the left side of the horizontal axis ($\lambda = 0$) is the pure LCBOPI⁺, on the right side ($\lambda = 1$) is the reference system, i.e. the Lennard-Jones liquid for the liquid phase and two Einstein crystals (with different coupling constant) for graphite and diamond. The simulated ten points per phase are marked by their error bars, that are almost reduced to a single dash at this scale.

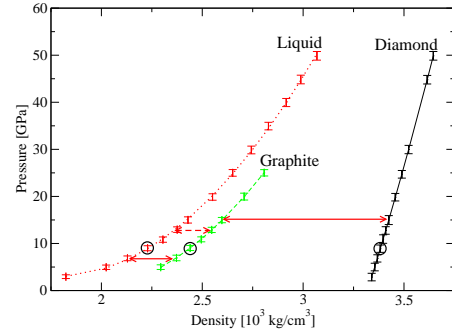


Figure 6: Equations of state at 4000K for the liquid, graphite, and diamond. The curves are quadratic polynomial fits to the data. The circles indicate the points, at 10 GPa, for which the Helmholtz free energy was determined using Eq. 6. The solid arrows connect coexisting (stable) points, i.e. liquid/graphite and graphite/diamond. The dashed arrow indicates the liquid/diamond coexisting point, with graphite metastable.

reference system (the absence of such transitions is a necessary condition for using this method). At the initial state point ($P = 10 \text{ GPa}$, $T = 4000 \text{ K}$), the calculated free energies ($\beta F^\boxtimes/N$) where -24.824 ± 0.006 , -24.583 ± 0.002 , and -25.137 ± 0.002 , for graphite, diamond, and the liquid, respectively.

Fig. 6 shows the calculated state points along the 4000 K isotherms for the three phases, along with

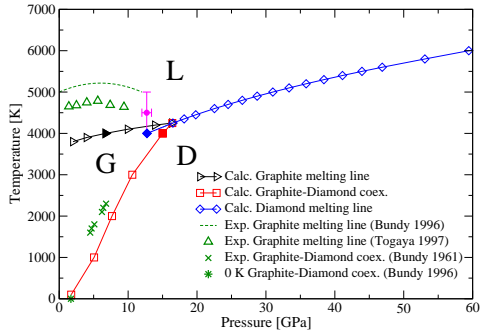


Figure 7: Phase diagram of carbon up to 60 GPa. The solid right triangle, square, and diamond are the three coexistence points found by equating the chemical potentials at 4000 K (see text). The open right triangles, squares, and diamonds are the calculated coexistence points, propagated via Gibbs-Duhem integration. The solid circle with error bars indicates the experimental estimate for the liquid/graphite/diamond triple point [73, 103, 99]. The dashed curve is the experimental graphite melting curve from Ref. [73]. The up triangles are graphite melting state points from Ref. [74]. The crosses represent experimental estimates for graphite/diamond coexistence from Ref. [80]. The asterisk represent the theoretical graphite/diamond coexistence at zero kelvin, as reported in Ref. [73].

the fitted curves. The fit parameters are listed in Table 1. Employing subsequently Eq. 7 we obtained the calculated chemical potential μ along the 4000 K isotherm for the liquid, graphite, and diamond phase. The intersections of the chemical potential curves yield the graphite/liquid coexistence at 6.72 ± 0.60 GPa ($\mu_{GL} = -24.21 \pm 0.10 k_B T$), and the graphite/diamond coexistence at 15.05 ± 0.30 GPa ($\mu_{GD} = -23.01 \pm 0.03 k_B T$). The third intersection locates a diamond/liquid coexistence at 12.75 ± 0.20 GPa ($\mu_{DL} = -23.24 \pm 0.03 k_B T$). Even though both diamond and the liquid are there metastable, the Clausius-Clapeyron integration of the diamond melting curve can be started at the metastable coexistence point at 4000K. Starting from the three coexistence points at 4000 K, the coexistence curves were traced by integrating the Clausius-Clapeyron equation using the trapezoidal-rule predictor-corrector scheme [100]. The new value of the coexisting P at a given T was taken when two iterations differed less than 0.01 GPa, this being the size of the single uncertainty in the calculation of dP/dT . Typically this required 2-3 iterations.

The calculated phase diagram in the $P - T$ plane is shown in Fig. 7 for the low pressure region, and in Fig. 8 for the pressures up to 400GPa. Tab. 2 lists the

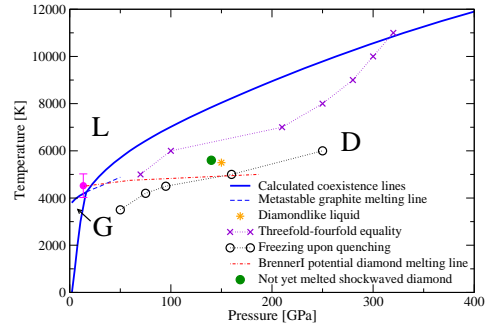


Figure 8: Phase diagram of carbon at between 0 and 400 GPa. The thick solid curves are our calculated phase boundaries. The dashed curve is the metastable prolongation of the graphite melting curve, from Gibbs-Duhem integration; the curve stops just before the simulated graphite became unstable, displaying large density fluctuations. The dashed-dotted curve departing from the experimental estimate for the triple point (solid circle with error bar [73, 103, 99]) is the diamond melting curve calculated in Ref. [104] with the BrennerI potential. The solid circle is the final point of the shock wave experiment of Ref. [93] at which diamond is not yet melted. The crosses mark the (metastable) liquid state points with an equal fraction of three and four-fold coordinated atoms. The circles represent state points at which the liquid freezes.

densities of selected points on the coexistence curves. The three coexistence curves meet in a triple point at 16.4 ± 0.7 GPa and 4250 ± 10 K.

The graphite/diamond coexistence curve agrees well with the experimental data. In the region near the liquid/graphite/diamond triple point that has not been directly probed in experiments, the graphite/diamond coexistence curve bends to the right, departing from the commonly assumed straight line. Analysis of our data shows this is mainly due to the rapid reduction with increasing pressure of the interplanar distance in graphite at those premelting temperature. This causes an enhanced increase of the density in graphite, yielding a decrease of dT/dP .

Table 2 shows the melting enthalpy Δh_m for graphite and diamond. These are calculated as the difference in enthalpy between the solid and the liquid at coexistence. Our calculated melting enthalpies of graphite are significantly lower than the values of ~ 110 kJ/mol that were reported in recent shock-heating melting experiments [73, 74]. Nonetheless our values retain the feature of being rather constant along the graphite melting curve. To our knowledge, no experimental data have been reported for the melting enthalpies of dia-

Graphite melting curve				
P [GPa]	T [K]	ρ_G	ρ_L	Δh_m
2.00	3800	2.134	1.759	68.8
6.70	4000	2.354	2.098	66.3
16.4	4250	2.623	2.414	64.7
Diamond melting curve				
P [GPa]	T [K]	ρ_D	ρ_L	Δh_m
16.4	4250	3.427	2.414	95.9
25.5	4750	3.470	2.607	111.5
43.9	5500	3.558	2.870	130.8
59.4	6000	3.629	3.043	143.9
99.4	7000	3.783	3.264	160.5
148.1	8000	3.960	3.485	164.7
263.2	10000	4.286	3.868	195.3
330.5	11000	4.230	4.045	208.1
408.1	12000	4.593	4.236	221.7

Table 2: Pressure (P), temperature (T), solid and liquid densities (ρ), and melting enthalpy (Δh_m) along the melting curves. Densities are expressed in 10^3 kg/m^3 , enthalpies are in [kJ/mol].

mond. Note, that they monotonically increase with temperature.

The calculated graphite melting temperature is monotonically increasing with pressure and is confined to small temperature range around 4000 K. In contrast to data inferred from experiments it shows no maximum and is at a somewhat lower temperature. In agreement with the experiments the coexistence temperature is only slowly varying with pressure. Inspection reveals that this behavior is due to a limited variability of the melting enthalpy, and a similar bulk modulus for liquid and graphite yielding a volume change upon melting that is almost constant along the melting curve.

The sign of the slope of the diamond melting curve is consistent with the available experimental data [93, 73] (see Fig. 8). When compared to the diamond melting curve of the BrennerI model [104], the LCBOP⁺ diamond melting curve has a steeper slope yielding significantly higher temperatures for the diamond melting curve. Recently, the melting curve of diamond in a range up to 2000 GPa has been studied by ab initio MD simulations using density functional theory. Wang et al. [105] determined the relative stability of the diamond and liquid phase by evaluating the free energy of both phases. Correa et al. [106] determined the melting temperature using a “two phase” simulation method, where the system initially consists of a liquid and a diamond structure that are in contact. Subsequently the

melting temperature is estimated by locating the temperature at which the system spontaneously evolves towards a liquid or a crystalline structure. In both ab initio MD studies it was found that the diamond melting curve shows a maximum; around 450 GPa [106] or 630 GPa [105]¹. Subsequent laser-shock experiments [107] provided data consistent with this observation, indicating a negative melting slope most probably in the region of 300-500 GPa. When comparing the LCBOP⁺ diamond melting curve, that monotonically increases with pressure, to the ab initio MD results of Refs. [105, 106] we see a significant deviation from 200 GPa onwards. This might be attributed to an incorrect description of the liquid structure at high compression. Indeed, LCBOP⁺ has not been validated against high density structures with coordination beyond four. These are typical configuration that might become more dominant in the pressure region beyond 200 GPa.

4 Existence of a liquid–liquid phase transition?

4.1 History of the LLPT near the graphite melting line

Analysis of experimental data The possibility of a LLPT in liquid carbon was first investigated by Korsunskaya *et al.* [36], who analysed data on the graphite melting curve proposed by Bundy [65], (those data showed a maximum melting temperature at 6.5 GPa). By fitting the data from Bundy into the original two levels model of Kittel [34] and postulating the existence of two liquids, Korsunskaya *et al.* found the critical temperature T_c of the LLPT. The model is fitted with *three* points on the graphite melting curve, with the respective derivatives, and with the heat of melting at *one* selected pressure. The fitting procedure gives an estimate for the critical pressure of ~ 6.5 GPa and for the critical temperature of the searched transition at 3770 K, i.e. below the melting temperature. The fitted value for the entropy of freezing is the same for the two liquids, thus implying a vertical slope (dT/dP) of the coexistence curve (in the metastable liquid region just below the critical temperature)

On the basis of these results, the authors were able to calculate also the diamond melting curve: they predicted it to have a negative slope, in accordance with

¹The difference between these two values gives a hint on the uncertainties related to the two different methods used for calculating coexistence, given that the DF-MD set-up is quite similar in the two works

the commonly accepted interpretation of the experiments of Alder and Christian [79]. Note that the slope of the *graphite* melting curve, and the slope of the diamond/graphite coexistence, as extracted from Bundy’s data [80, 65], together with the densities of the phases obtained by fitting to the two levels model *implied* (via Clausius-Clapeyron equation) a negative slope of the diamond melting curve. Different values of the slopes of the graphite boundary curves, and of the densities of the phases can yield rather different slope of the diamond melting curve.

Consistent with the slope of the fitted graphite melting curve, the low density liquid is predicted less dense than the coexisting graphite, and the high density liquid more dense than the coexisting graphite. The nature of the two liquids was predicted as follows: at low pressure graphite melts into a liquid of neutral particles that interact predominantly through dispersion (London) forces. Upon increasing pressure the liquid would transform into a metallic close packed liquid. No assumptions were made on the local structure.

A semi-empirical equation of state The modern discussion on the LLPT for carbon, starts with the elaboration of a semi-empirical equation of state for carbon, valid also at high P and T , by van Thiel and Ree [108, 99]. This equation of state was constructed on the basis of experimental data and electronic structure calculations. It postulated the existence, in the graphite melt, of a mixture of an sp_2 and an sp_3 liquid. By assuming the model of *pseudo-binary mixture* for the description of the mixing of the two liquids [38], Van Thiel and Ree showed that fitting their empirical equation of state to the graphite melting points of Bundy [65], they predict a graphite melting curve that shows a maximum with a discontinuous change of the slope, so that a first order LLPT arises. On the other hand, if they fit their model to the data from Ref. [109], the predicted T_c of the LLPT drops below the melting curve and the transition between the two liquids becomes continuous in the stable liquid region. As pointed out by Ponyatovsky [110] the expression for the mixing energy of the two liquid as proposed by van Thiel and Ree in [108, 99] involves two ambiguities. Firstly, extrapolating the coexistence curve between the two liquids at atmospheric pressure, the coexistence temperature would be $T \sim 3700$ K: this would imply that the sp_3 liquid (and the glass) would be more stable than the sp_2 at ambient pressure up to very high temperatures, which is in disagreement with the experimental data. Furthermore, the mixing energy is proposed to have a linear dependence on T , so that, when $T \rightarrow 0$, also the mixing energy would tend to zero, i.e. at zero temperature the regular solution

would become an ideal solution. This would be rather unusual.

Experimental evidence from the graphite melting curve Using flash-heating experiments Togaya [74] determined the melting line of graphite and found a maximum in the melting curve at $P_{max} = 5.6$ GPa. This author fitted the six experimental points with two straight lines: with positive slope at pressures lower than P_{max} , with negative slope at pressures higher than P_{max} . The apparent discontinuity at the maximum would imply the presence of a triple point graphite/ low-density-liquid (LDL) / high-density-liquid (HDL), as a starting point of a LLPT coexistence curve.

Prediction of a short-range bond-order potential In Ref. [103] Glosli and Ree reported a complete study of a LLPT simulated with the ‘BrennerI’ bond-order potential [52] in its version with torsional interactions [111]. The authors simulated in the canonical (NVT) ensemble several samples at increasing densities at eight different temperatures. By measuring the pressure, they show the familiar van der Waals loop betraying mechanical instability over a finite density range. Using the Maxwell equal-area construction, the authors calculated the LLPT coexistence curve, ending in a critical point at $T = 8802$ K and $P = 10.56$ GPa. The lowest temperature coexistence point was calculated at $T = 5500$ K and $P = 2.696$ GPa. The LDL/HDL coexistence curve should meet the graphite melting curve at its maximum, but unfortunately the BrennerI potential does not contain non bonded interactions, thus it can describe neither bulk graphite nor its melting curve. To overcome this deficiency, the authors devised an ingenious perturbation method. Assuming constant slope of the negative sloped branch of the graphite melting curve (the authors adopted the graphite melting curve measured by Togaya [74]) and fixing the graphite/diamond/HDL triple point at a value taken from the experimental literature, they give an estimate of the graphite/LDL/HDL triple point, at $T = 5133$ K and $P = 1.88$ GPa. The LDL was found to be mainly two-fold (sp) coordinated with a polymeric-like structure, while the HDL was found to be a network forming, mainly four-fold, (sp_3) liquid. Following the predictions of this bond-order potential, the sp_2 coordinated atoms would be completely avoided in the liquid. The authors identified the reason in the presence of torsional interactions. In fact, the increase in density demands an increase in structures with higher coordination than the sp , which is entropically favored at low densities. The single bonds of the sp_3 structures can freely rotate around the bond axis, while bonds between sp_2 sites are constrained in a (almost) planar

geometry by the torsional interactions: this implies a low entropy for a liquid dominated by sp_2 sites. This low entropy would eventually destabilize the sp_2 sites towards the sp_3 . To prove this conjecture, the authors calculated two relevant isotherms in the original version of the potential, without torsional interactions, finding no sign of a LLPT. Since some torsional interactions are definitely needed to mimic the double bond reluctance to twist, the authors concluded that the LLPT predicted by the Brenner bond-order potential with torsion is more realistic than its absence when torsional interactions are switched off.

Tight binding calculations [112] showed no evidence of van der Waals loops at some of the temperatures analyzed in Ref. [103]. As Glosli and Ree note, the tight binding model used in [112] is strictly two-center, thus the torsional interactions *cannot* be described.

An ab initio study of the LLPT In Ref. [45], Wu *et al.* reported a series of NVT-CPMD simulations at 6000 K from density 1.27 to $3.02 \cdot 10^3$ kg/m³, in a range where the BrennerI potential showed the first order LLPT at the same T . No sign of a van der Waals loop was found: in contrast to the BrennerI results of the previous paragraph, two approaching series starting from the lowest and the highest density, were found to meet smoothly at intermediate densities. Looking for the reasons of the failure of the BrennerI potential, the authors calculated, with the same functional used in the CPMD simulations, the torsional energy of two model molecules. One, $(\text{CH}_3)_2\text{C}=\text{C}(\text{CH}_3)_2$, was chosen so that the bond between the two central atoms represents a double bond in a carbon network: two sp_2 sites are bonded each to two sp_3 sites; the peripheral hydrogens are needed to saturate the sp_3 atoms and are intended to have no effect on the central bond. The second molecule, $(\text{CH}_2)_2\text{C}-\text{C}(\text{CH}_2)_2$ is a portion of a completely sp_2 coordinated network: in the bond-order language, the central bond is conjugated. The two molecules were geometrically optimized in their planar configurations and then twisted around the central bond axis in steps of $\pi/12$. In each configuration the electronic wave function was optimized, without further relaxations, to give the total energy, that was compared to the planar configuration total energy. The difference is the torsional energy. The DF calculations found a surprising picture: while the double bond torsional energy was only slightly overestimated by the BrennerI potential at intermediate angles, the DF torsional energy for the conjugated bond showed a completely different scenario compared to the classical prediction. It shows a maximum at $\pi/4$, while the planar and orthogonal configuration have basically the same energy. For the BrennerI potential, the torsional en-

ergy in this conjugated configuration is monotonically increasing with the torsion angle, just as for the double bond configuration. On average, considering that the conjugated configuration would be characteristic of a mainly sp_2 coordinated liquid, the torsional interactions are enormously overestimated by the classical potential. As a further illustration, the authors tried to lower torsional energy of the conjugated bond in the classical potential, by tuning the proper parameter, and found a much less pronounced LLPT. Note that the functional form of the torsional interactions for the BrennerI potential *cannot* reproduce the DF data mentioned here. Wu *et al.* concluded that “[the] Brenner potential significantly overestimates the torsional barrier of a chemical bond between two- and three-center-coordinated carbon atoms due to the inability of the potential to describe lone pair electrons”; and: “[the] Brenner potential parameters derived from isolated hydrocarbon molecules and used in the literature to simulate various carbon systems may not be adequate to use for condensed phases, especially so in the presence of lone pair electrons”. In the next section we show that the conclusion of Wu *et al.* is not necessarily true for all BOPs; indeed, LCBOP⁺, the carbon bond-order potential proposed by Los and Fasolino (see section 2), includes a definition of the torsional interaction which is able to reproduce relevant features of liquid carbon, as they are described by DF-MD.

4.2 Ruling out the LLPT in the stable liquid region via LCBOP

We have already indicated that the change of the structure of the liquid along the graphite and diamond melting curve is related to the slope of the melting curve. More importantly, it plays also a crucial role in the nucleation of diamond in liquid carbon. The latter will be further discussed in the next section.

The calculated melting curves of the LCBOP⁺ model for carbon up to 400 GPa provide strong evidence that there is no LLPT in the stable liquid phase. One indication is the smoothness of the slopes of the melting curves. A further argument lies in the structure of the liquid near freezing. Below we discuss this in more detail.

The calculated phase diagram (Figs. 7 and 8) does not show the sharp maximum in the graphite melting line that was inferred from the calculated first-order LLPT for the BrennerI bond-order potential[103]. As we mentioned in the previous section, subsequent DF-MD simulations of liquid carbon [45, 46] indicate that the BrennerI LLPT is spurious: it originates from an inadequate description of the torsional contribution to

the interactions. We have extended the calculation of the graphite melting curve of LCBOP⁺ towards higher pressures into the region where both graphite and the liquid are metastable with respect to diamond. It is plotted as a dashed curve in Fig. 8 that shows the same trend as at lower pressures. Hence, the calculated slope of the graphite melting curve is incompatible with the existence of a LLPT in this region of the carbon phase diagram.

In order to further analyze the nature of the liquid, we determined several structural properties of the liquid near the melting curve where we also explored the diamond melting curve. Fig. 9 shows the coordination fraction in the liquid along the coexistence curves up to 400 GPa, as function of temperature, pressure and density, with a linear scale in density. The dashed curve is the calculated graphite/diamond/liquid triple point. Along the graphite melting curve, the three-fold and two-fold coordination fractions remain rather constant, with the four-fold coordination slightly increasing to account for the increase in density. Along the diamond melting curve the three-fold coordinated atoms are gradually replaced by four-fold coordinated atoms. However, only at (3.9 10³ kg/m³, 300 GPa, and 10500 K) the liquid has an equal fraction of three-fold and four-fold coordinated atoms. The change of dominant coordination is rather smooth. Moreover, we have verified that it is fully reversible showing no sign of hysteresis in the region around the swapping of dominant coordination. We note, that these results contradict the generally assumed picture (see e.g. Ref. [99]) that diamond melts into a four-fold coordinated liquid. Our calculations suggest that up to ~300 GPa the three-fold coordination dominates.

The interrelation between three and four-fold sites, was further investigated calculating the partial radial distribution functions ($g_{ij}(r)$) of the liquid at 300 GPa, and 10500 K. Partial radial distribution functions are defined as the probability of finding a j -fold site at a distance r from a i -fold site; the total radial distribution function g is recovered by: $g = \sum_i g_{ii} + 2 \sum_{i \neq j} g_{ij}$. We show the results in Fig. 10; we focus on the three predominant curves, describing the pair correlations between three-fold atoms (g_{33}), between four-fold atoms (g_{44}), and the cross pair correlation between three- and four-fold sites (g_{34}). Disregarding the rather pronounced minimum in correspondence of the dip around 2 Å of the g_{33} and the g_{34} , the similarity of three curves at all distances r is striking. The two sites are almost undistinguishable: in case of a tendency towards a phase transition, one would expect some segregation of the two structures. In contrast, looking at distances within the first neighbours shell, a

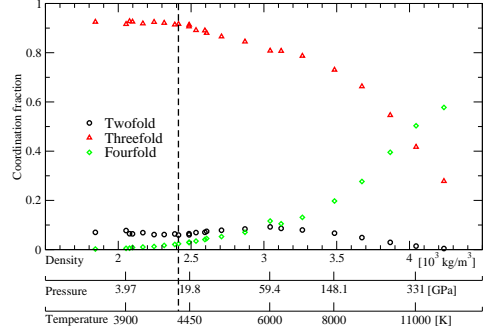


Figure 9: Coordination fraction of the liquid along the melting curve of carbon. The melting curves are unimodal, thus fixing ρ providing one-to-one relation among ρ , P and T . The scale for ρ is chosen to be linear. The dashed curve is the liquid/graphite/diamond triple point. On the left hand side of the triple point, the liquid coexists with graphite, while on the right hand side it coexists with diamond.

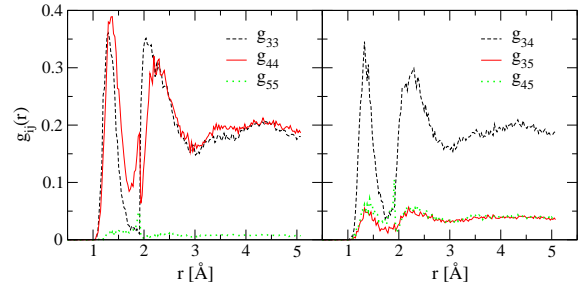


Figure 10: Partial distribution functions g_{ij} of the liquid at the calculated coexistence with diamond, at 10500 K and ~ 300 GPa, when three- and four-fold atoms are equally present. The left panel is for the diagonal contributions (i.e. for $i = j$), while the right panel is for the cross correlations (i.e. for $i \neq j$).

three-fold site seems to bond indifferently to a three- or a four-fold site, and viceversa. Furthermore, the partial structures up to the third, quite pronounced, peak at ~ 4.5 Å, are almost the same for these three partial radial distribution functions.

We determined the properties of the metastable liquid in the stable diamond region. Fig. 8 shows the liquid $P - T$ state points (crosses) that exhibit an equal number of three and four-fold coordinated atoms. It ranges from the high-pressure high-temperature region where the liquid is thermodynamically stable down into the diamond region, where the liquid is metastable for the LCBOP. The circles indicate state points in which the LCBOP liquid freezes in the simulation. Enclosed by the two set of points lies what we baptized diamond-

like liquid. This is a mainly four-fold coordinated liquid with a rather pronounced diamond-like structure in the first coordination shell and was discussed in [46]. This suggests that a (meta)stable liquid with a dominantly four-fold coordination may only exist for pressures beyond ≈ 100 GPa and could imply that the freezing of liquid into a diamond structure might be severely hindered for a large range of pressures beyond the graphite/diamond/liquid triple point. In Ref. [46] it is also pointed out that at 6000 K the equation of state shows a change of slope around the transition to the four-fold liquid. At even lower temperature this feature becomes more and more evident, but for temperatures lower than ~ 4500 K the liquid freezes into a mainly four-fold coordinated amorphous structure. This observation is consistent with quenching MD simulations [113, 114] to obtain the tetrahedral amorphous carbon. In those simulations a mainly three-fold liquid freezes into an almost completely four-fold amorphous.

Recent fully ab-initio study of the diamond melting line [105, 106] predicted a maximum at pressures beyond the maximum pressure (400 GPa) we explored with our potential. The maximum implies a liquid denser than diamond at pressure higher than the pressure at which the maximum appears. The authors of both works analyzed the structure of the liquid around this maximum, finding no sign of abrupt change in density and/or coordination. This points towards excluding a LLPT between a four-fold and a higher-fold coordinate liquid; rather, a smooth transformation towards a denser liquid is always observed.

5 Diamond nucleation

Our knowledge of the phase diagram of “LCBOPI+ carbon” allows us to identify the regions of the phase diagram where diamond nucleation may occur. We studied the homogeneous nucleation of diamond from bulk liquid, by computing the steady-state nucleation rate and analyzing the pathways to diamond formation. On the basis of our calculations, we speculate that the mechanism for nucleation control is relevant for crystallization in many network-forming liquids, and also estimate the conditions under which homogeneous diamond nucleation is likely in carbon-rich stars and planets such as Uranus and Neptune.

Steady-state nucleation rate Most liquids can be cooled considerably below their equilibrium freezing point before crystals start to form spontaneously in the bulk. This is caused by the fact that microscopic crystallites are thermodynamically less stable than the bulk solid. Spontaneous crystal growth can only proceed when, due to some rare fluctuation, one

or more micro-crystallites exceed a critical size (the “critical cluster”): this phenomenon is called homogeneous nucleation. An estimate of the free-energy barrier the system has to cross in order to form critical clusters and of the rate at which those clusters form in a bulk super-cooled liquid, can be obtained from Classical Nucleation Theory (CNT) [115]. CNT assumes that $\Delta G(n)$, the Gibbs free-energy difference between the metastable liquid containing an n -particle crystal cluster and the pure liquid, is given by

$$\Delta G(n) = S(n)\gamma - n|\Delta\mu|, \quad (8)$$

where $S(n)$ is the area of the interface between an n -particle crystallite and the metastable liquid, γ is the liquid-solid surface free-energy per unit area, and $\Delta\mu$ the difference in chemical potential between the solid and the super-cooled liquid. The surface area $S(n)$ is proportional to $c(n/\rho_S)^{2/3}$, where the factor c depends on the shape and the geometry of the cluster (e.g. $c = 16\pi/3$ for a spherical cluster).

The top of the free-energy barrier ΔG^* to grow the crystalline critical cluster is then given by

$$\Delta G^* = c \frac{\gamma^3}{\rho_S^2 |\Delta\mu|^2}, \quad (9)$$

where ρ_S is the number density of the stable phase and c indicates the geometrical properties of the growing cluster. From our simulations, we can only determine the product $c\gamma$: it is this quantity and the degree of super-saturation ($\Delta\mu$), that are needed to compute the top of the free-energy barrier, and hence the nucleation rate.

CNT relates R , the steady-state nucleation rate, i.e. the number of crystal clusters that form per second per cubic meter, to ΔG^* , the height of the free-energy barrier that has to be crossed to nucleate the critical crystal n^* :

$$R^{CNT} = \kappa e^{-\beta\Delta G(n^*)}, \quad (10)$$

where ΔG^* is the top of the free-energy barrier and κ is the kinetic prefactor. The kinetic prefactor term is defined as

$$\kappa = \rho_L k_{+,n^*} Z \quad (11)$$

where ρ_L is the liquid number density, k_{+,n^*} the attachment rate of single particles to a spherical crystalline cluster $k_{+,n^*} = (24D(n^*)^{2/3})/\lambda^2$, with D/λ^2 proportional to the jump frequency (λ being the atomic jump distance) and $Z = \sqrt{|\Delta\mu|/(6\pi k_B T n^*)}$ the so-called Zeldovitch factor. As the nucleation rate depends exponentially on ΔG^* , a doubling of γ may change the nucleation rate by many orders of magnitude.

Because of the extreme conditions under which homogeneous diamond nucleation takes place, there have been no quantitative experimental studies to determine its rate. Moreover, there exist no numerical estimates of $\Delta\mu$ and γ for diamond in super-cooled liquid carbon. Hence, it was thus far impossible to make even an order-of-magnitude estimate of the rate of diamond nucleation.

Results We simulate a 2744 particles bulk liquid carbon using periodic boundary conditions, with a cubic box whose edge is 18Å. We make it metastable by undercooling it at constant pressure at two different state points, $A\{P = 85 \text{ GPa}, T = 5000 \text{ K}\}$ and $B\{P = 30 \text{ GPa}, T = 3750 \text{ K}\}$. At both state points, the liquid is super-cooled by $(T_m - T)/T_m \approx 25\%$ below the diamond melting curve, T_m being the melting temperature $T_m^A = 6600 \text{ K}$ and $T_m^B = 5000 \text{ K}$, respectively.

We evaluate $\Delta\mu$ by thermodynamic integration at constant pressure from the melting point ($\beta_M = 1/k_B T_M$)

$$\Delta(\beta_i \mu) = \int_{\beta_M}^{\beta_i} \langle [h_S(\beta) - h_L(\beta)] \rangle_P d\beta \quad (12)$$

where $\beta_i = 1/k_B T_i$, $\{i = A, B\}$, and h is the enthalpy per particle of the solid and liquid phase, respectively. We then find: $|\Delta\mu_A/k_B T| = 0.60$ and $|\Delta\mu_B/k_B T| = 0.77$.

In recent years several authors have been developing methods for studying homogeneous nucleation from the bulk and detecting solid particles within the metastable liquid [116, 117, 118, 119]. Our study on diamond nucleation is based on these works, but it requires various adaptations due to the specificity of the carbon covalent bond [55]. We have already shown that liquid carbon is rather structured below its freezing curve. This leads to the need of building a "strict" definition of "crystallinity" of a particle, in order to avoid an overestimation of the number of solid particles in the system.

In order to compute the nucleation free energy, we use the biggest crystal cluster n as a local order parameter to quantify the transformation from the liquid to the solid. To identify solid-like particles, we analyze the local environment of a particle using a criterion based on a spherical-harmonics expansion of the local bond order. In practice, the present bond-order parameter is based on rotational invariants constructed out of rank three spherical harmonics (Y_{3m}). This choice allows us to identify the tetragonal symmetry of the diamond structure, as already described in Ref. [55, 119], and it is also perfectly suited to find particles in a graphite-like environment. Our choice of odd-order of spherical

harmonics is due to the fact that both diamond and graphite lattices have odd symmetry upon inversion of coordinates.

In order to define the local order parameter, we start with computing

$$q_{3,m}(i) = \frac{1}{Z_i} \sum_{j \neq i} S^{down}(r_{ij}) Y_{3m}(\hat{\mathbf{r}}_{ij}) \quad (13)$$

where the sum extends over all neighbors of particle i and over all values of m . Z_i is the fractional number of neighbours and $S^{down}(r_{ij})$ is a smooth cut-off function, introduced in the context of *LCBOPI*⁺[55] (see also Section II.A in [40]).

By properly normalizing Eq. 13, we get

$$q'_{3,m}(i) = \frac{q_{3,m}(i)}{(\sum_{m=-l}^l q_{3,m}(i) \cdot q_{3,m}^*(i))^{1/2}}, \quad (14)$$

being $q_{3,m}^*$ the complex conjugate of $q_{3,m}$.

Next we define the dot product between the normalized function $q'_{3,m}$ of particle i and the same function computed for each of its first neighbors, $d_3(i, j)$, and sum them up over all the m values:

$$d_3(i, j) = \sum_{m=-l}^l q'_{3,m}(i) \cdot q'_{3,m}(j) S^{down}(r_{ij}). \quad (15)$$

$d_3(i, j)$ is a real number defined between -1 and 1: it assumes the value of -1 when computed for both graphite and diamond ideal structures.

Two neighboring particles i and j are considered to be connected whenever $d_3(i, j) \leq d_c = -0.87$. This value satisfactorily splits the distributions of solid particles belonging to a thermalized lattice and liquid particles as found in a liquid. The histograms that led us to this choice are thoroughly discussed in Refs. [55, 119]. By counting the total number of connections (n_{con}) and plotting the probability distribution of n_{con} , we define a threshold for the number of connections needed to neatly distinguish between a liquid-like and a solid-like environment: we assume that whenever $n_{con} > n_{con}^c = 3$ a particle is solid-like. At this stage, we do not specify any nature of the particle's crystallinity, whether diamond-like or graphite-like. By means of a cluster algorithm we then define all the solid-like AND connected particles as belonging to the same crystal cluster. After computing the size of each cluster, we use the size of the biggest cluster as the order parameter which describes the phase transition [120].

Once properly identified the biggest crystalline cluster in the system, we use the umbrella sampling technique [121] to measure the free-energy barrier ΔG^* to

form a critical cluster at state point A . In order to better equilibrate the growing clusters, we implement a “parallel tempering” algorithm similar to the one described in Ref. [122]. We obtain that, at state point A , ΔG_A^* is around $25 k_B T$ for a critical cluster size of $n_A = 110$. By fitting the initial slope of Eq. 8 to a polynomial function assuming a spherical growing cluster, while imposing the value of the correspondent super-saturation ($\beta\Delta\mu = 0.60$), the inter-facial free energy is $\gamma_A = 0.27k_B T/\text{\AA}^2 \simeq 1.86 \text{ J m}^{-2}$. The same value of γ_A is obtained from the top of the free-energy barrier assuming a spherical cluster shape (Eq. 9) ($\rho_S = 0.191 \text{ \AA}^{-3}$). We underline the fact that at the chosen thermodynamic conditions, there are no finite size effects, caused by *spurious* interaction of the critical cluster with its own periodically repeated image.

By knowing the inter-facial free energy in A , and assuming the validity of CNT, we estimate the crystal nucleation rate by means of Eq. 10, where we use Eq. 11 to compute the kinetic pre-factor (the atomic jump distance λ being of the order of the diamond bond distance, 1.54\AA): $R_A^{CNT} \sim O(10^{30}) \text{ s}^{-1}\text{m}^{-3}$.

We also use Forward-Flux Sampling (FFS), a relatively recent rare events technique useful to compute the nucleation rate and to study the pathways to nucleation [123, 124, 119], and we measure the crystal nucleation rate at state point A . FFS yields an estimate for the nucleation rate that is three orders of magnitude higher than the one estimated by means of Eq. 10. Whilst such a discrepancy seems large, it need not be significant because nucleation rates are extremely sensitive to small errors in the calculation of the nucleation barrier. Two possible reasons for this discrepancy are: 1) if we consider that the standard deviation corresponding to γ is around 10% of its measured value, we conclude that the nucleation rate is $O(10^{30\pm 3}) \text{ s}^{-1}\text{m}^{-3}$; 2) another source of error can be the poor statistics when computing the nucleation rate from molten carbon by means of FFS. This is due to the time consuming calculations of the interaction potential: in our study we are in fact forced to base our results on $O(10)$ independent nucleation events. Fig. 11 shows a typical critical cluster at state point A obtained in the FFS simulations: it contains around 110 particles, and it is surrounded by mainly 4-fold coordinated liquid particles. The picture shows two different views of the same cluster: it appears evident that all particles within the bulk are diamond-like, whereas the particles belonging to the outer surface are less connected but still mainly 3-4 fold coordinated.

We then attempt to compute the nucleation rate at state point B by means of FFS and, even in rather long simulations, we cannot observe the formation of

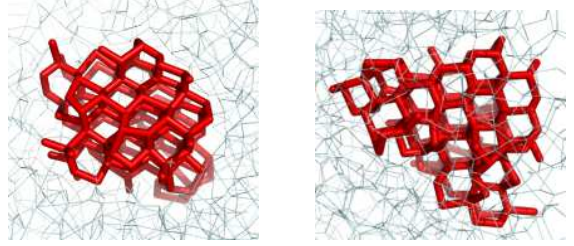


Figure 11: Two different views of the biggest cluster at state point A containing around 110 particles, surrounded by mainly 4-fold coordinated liquid particles.

any crystal cluster containing more than 75 particles. Hence, these calculations suggest that the nucleation rate at state point B measured by means of FFS is around zero. Figure 12 shows a 75 particles cluster con-

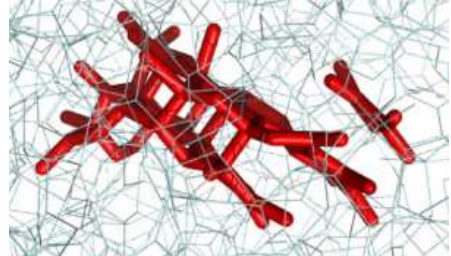


Figure 12: Typical snapshot of a crystalline cluster of ~ 75 particles obtained at state point B , surrounded by mainly 3-fold coordinated liquid particles.

taining 3-fold coordinated surface particles surrounding the 4-fold coordinated bulk particles, while embedded in a 2-3 fold coordinated liquid.

As we are unable to grow critical nuclei with FFS, we assume that a system of 2744 particles is too small to accommodate a spherical critical cluster. According to Classical Nucleation Theory (CNT) [115], the crystal nucleation rate depends exponentially on the height of the free-energy barrier (see Eq. 10). The latter is a function of the inter-facial free energy (γ) cube and inversely proportional to the super-saturation ($\Delta\mu$) square. Since the super-saturation is quite similar in both state points, the failure of the system to nucleate suggests that the inter-facial free energy should play a major role. In order to estimate the free-energy barrier in state point B , as we know the solid number density ($\rho_S = 0.177 \text{ \AA}^{-3}$) and the chemical potential difference between the liquid and the solid ($\beta\Delta\mu_B = 0.77$), we only need to calculate the inter-facial free energy γ . Thus, in what follows, we focus on methods to estimate

γ at state point B .

As a spherical critical cluster does not fit in our simulation box, we prepare a rod-like crystal in a system with a slab geometry: this is a flattened box containing around 4000 particles, with lateral dimensions that are some four times larger than its height. The crystal rod is oriented perpendicular to the plane of the slab, it spans the height of the simulation box and is continued periodically. The cross section of this crystal rod is initially lozenge shaped, such that its [111]-faces are in contact with the liquid. The [111]-planes are the most stable ones for the diamond lattice. In fact, macroscopic natural diamonds have often an octahedral shape, with eight [111]-exposed surfaces. Indeed, we find stable [111] surfaces in all but the smallest studied diamond clusters.

At state point A clusters grow by the addition of particles to the surface made of mainly [111]-planes. Note that when graphite and diamond structures compete at state point B (as shown in Fig. 12), the [0001]-graphite sheets transform into [111] diamond planes. Fig. 13 represents the top view at state point B of a

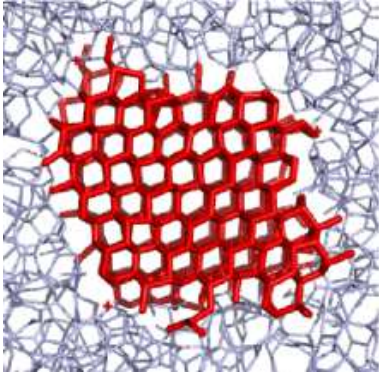


Figure 13: Top view of a rectangular parallelepiped formed by 4 [111]-faces and 2 [1-10]-lozenge bases with an acute angle $\theta=70.52$ degrees thermalized at state point B .

rod-like crystal, formed by 4 [111]-faces and 2 bases as [1-10]-lozenge with the acute angles of $\theta=70.52$ degrees. We then rewrite Eq. 8 for a rectangular parallelepiped having 4 faces and 2 lozenge-shaped basis

$$\Delta G = 4\sqrt{\frac{h}{\rho_S \sin \theta}} \gamma^l n^{1/2} - |\Delta \mu| n, \quad (16)$$

where h is the slab's height. We then use Umbrella Sampling to compute the initial slope of the free-energy barrier. As $h = 10 \text{ \AA}$, we obtain from fitting Eq. 16 that the inter-facial free energy for the lozenge-shaped cluster is $\gamma_B^l = 0.91 k_B T / \text{\AA}^2 \simeq 4.70$

J m^{-2} . At the same time, computing the inter-facial free energy of the rod-like crystal at state point A gives $\gamma_A^l = 0.37 k_B T / \text{\AA}^2 \simeq 2.55 \text{ J m}^{-2}$, considering the same slab's height and the same angle θ .

Now that we have estimates for the inter-facial free energies of the lozenge-shaped clusters at both state points A and B , we can estimate the ratio between them and find that $c\gamma_B/c\gamma_A = \gamma_B/\gamma_A \simeq 2.5$. As we compare clusters having the same shape, this ratio is presumably not very sensitive to the precise (and, a priori unknown) shape of the cluster shape. As the surface free energy at state point B is appreciably higher than at state point A , the early stages of crystal formation at point B are strongly suppressed by the inter-facial free-energy term. Since we know γ_A (referred to a hypothetical spherical cluster) and the ratio between the two γ 's, we can infer that the "effective" $\gamma_B = 0.68 k_B T / \text{\AA}^2 \simeq 3.50 \text{ J m}^{-2}$.

This value of the surface free energy is so large that we would indeed have needed a much larger system in order to accommodate the critical cluster at the state B thermodynamic conditions. From Eq. 16, we calculate the critical cluster size for the lozenge-shaped parallelepiped n_{2D}^* and use it to estimate the size of a critical spherical cluster n_{3D}^* in B :

$$n_{2D}^* = \frac{4h}{\rho_S \sin \theta} \frac{(\gamma)^2}{(\Delta \mu)^2}. \quad (17)$$

At state point B we find $n_{2D}^* \sim 330$ particles. Expressing n_{3D}^* as a function of the lozenge-shaped parallelepiped one, we get

$$n_{3D}^* = \frac{8}{3} \pi \frac{\gamma \sin \theta}{\rho_S \Delta \mu h} \times n_{2D}^*, \quad (18)$$

where ρ_S is the solid number density $\rho_B = 0.17 \text{ \AA}^{-3}$, $|\Delta \mu_B / k_B T| = 0.77$, and h the height of the slab (10 \AA). Thus, $n_{3D}^* \sim 1700$ particles at state point B . To guarantee that the critical cluster does not interact with its own periodic images, its radius should always be less than 25% of the box diameter L . A spherical cluster with a radius of $0.25 L$ occupies $\sim 7 \%$ of the volume of the box and, as the solid is denser than the liquid, it contains about 10 % of the total number of particles ($N \approx 17000$). Such a large system size is beyond our present computational capacity. In contrast, in the slab geometry we find that the free energy of a lozenge-shaped crystal goes through a maximum at a size of ~ 330 particles, which is much less than the system size (4000 particles).

As $\Delta \mu$ and ρ_B are known, we can now use CNT to estimate ΔG^* in state point B . It turns out that, mainly because γ_B is 2.5 times larger than γ_A , the nucleation

barrier in B is more than ten times higher than in point A , and the nucleation rate is $R_B \sim 10^{-80} \text{ s}^{-1} \text{ m}^{-3}$.

To understand the microscopic origin for the large difference in nucleation rates in state points A and B , it is useful to compare the local structure of the liquid phase in both state points. As discussed in section 4.1 above (see also [46, 125]), liquid carbon is mainly 4-fold coordinated at state point A (20% 3-fold and 80% 4-fold), whereas at the lower temperatures and pressures of point B , the coordination in the liquid resembles that of graphite and is mainly 3-fold coordinated (5% 2-fold, 85% 3-fold and 10% 4-fold).

We can analyze the structure of the crystalline clusters that form in the supersaturated liquid carbon and distinguish graphite-like from diamond-like particles. In an *a posteriori* analysis, we use a different order parameter function of the order two spherical harmonics, and particularly sensitive to the graphite planar geometry. $q_{2m}(i)$ is the linear combination of spherical harmonics computed for each particle i

$$q_{2m}(i) = \frac{1}{Z_i} \sum_{j \neq i} S^{\text{down}}(r_{ij}) Y_{2m}(\hat{\mathbf{r}}_{ij}) \quad (19)$$

where the sum extends over all neighbors of particle i . We then sum over all the m values and calculate the modulus, $|q_2|$. The $|q_2|$ probability distribution for both A and B is represented in Fig. 14. Figure 14 depicts the features of both the smallest (~ 20 in both state points A and B) and the biggest clusters (~ 250 in A and ~ 75 in B). We also distinguish among: liquid-like particles (circles), particles belonging to the surface of the largest cluster (squares), particles inside the bulk cluster (diamonds) and particles belonging to the first liquid layer surrounding the largest cluster (triangles). According to our definition, particles belonging to the surface of the cluster are those *connected* to solid-like particles, but not solid-like themselves. Concerning particles belonging to the first liquid layer surrounding the cluster, they usually display the same behaviour as the ones belonging to the cluster surface, which is not surprising in view of the uncertainty in distinguishing a surface-particle from a first-liquid-layer particle. To neatly distinguish between diamond-like or graphite-like environment, we use as a reference the $|q_2|$ probability distribution for both bulk diamond (D) and graphite (G) (inset of Fig. 14).

At state point A , it is clear that bulk particles belonging to small clusters (bottom-left side) and big clusters (bottom-right side) are mainly diamond-like, as well as particles belonging to the surface of the clusters. In contrast, at state point B bulk particles belonging to small clusters (top-left side) show both graphite-like and diamond-like finger-prints. By vi-

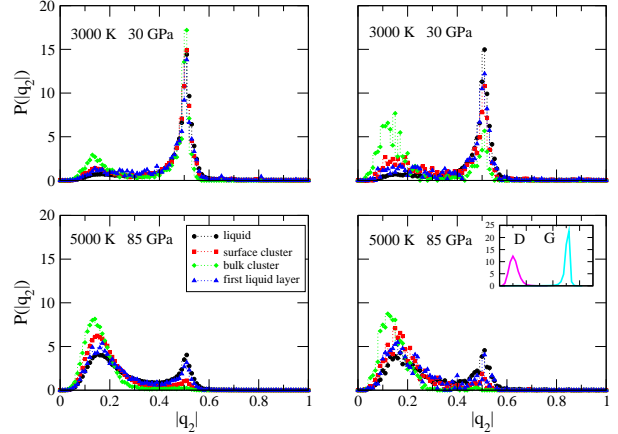


Figure 14: The top-left represents clusters of ~ 20 and the top-right clusters of ~ 75 at state point B , whereas the bottom-left clusters of ~ 20 and the bottom-right clusters of ~ 250 particles at state point A . The used code is: circles=liquid particles, squares=particles belonging to the biggest cluster’s surface, diamonds=particles within the bulk cluster, triangles=particles belonging to the first liquid layer surrounding the biggest cluster. The inset shows the $|q_2|$ probability distribution for an equilibrated bulk diamond (D) (left-hand side) and graphite (G) (right-hand side).

sual inspection, we note that when clusters grow larger (around 75 particles), particles at the surface tend to be mainly 3-fold coordinated, whereas bulk particles stay 4-fold coordinated, as shown in the top-right side of Fig. 14. The destabilizing effect of the graphitic liquid on the diamond clusters is most pronounced for small clusters (large surface-to-volume ratio): clusters containing less than 25 particles tend to be graphitic in structure, clusters containing up to 60 particles show a mixed graphite-diamond structure (see Fig. 12). It appears that the unusual surface structure of the diamond cluster is an indication of the poor match between a diamond lattice and a 3-fold coordinated liquid.

5.1 Consequences for other network forming liquids, carbon-rich stars, Uranus and Neptune

As discussed in the introduction, there are many network-forming liquids that, upon changing pressure and temperature, undergo profound structural changes or even LLPT [29, 23, 126]. Interestingly, our simulations show that the ease of homogeneous crystal nucleation at constant super-saturation from one-and-the-same meta-stable liquid can be tuned by changing its

pressure, and thereby its local structure.

Pressures and temperatures that we investigate for the diamond nucleation are in practice impossible to reach in experiments. However, such conditions are likely to be found in several extraterrestrial “laboratories”. Homogeneous nucleation of diamond may have taken place in the atmosphere of carbon-rich binary stellar systems comprising the so-called carbon stars and white dwarfs [127, 128]. Closer to home, it has been suggested that diamonds could also have formed in the carbon-rich middle layer of Uranus and Neptune [96, 129, 130] where, due to the high pressure and temperature, the relatively abundant CH_4 would decompose into its atomic components. In fact, experiments on methane laser-heated in diamond anvil cells [131] found evidence for diamond production. *Ab initio* simulations [132] also found that hot, compressed methane will dissociate to form diamond. Yet, there is a large discrepancy between the estimates of the pressures (and thus depth in the planet interior) at which the diamond formation would take place. The laser-heating experiments [131] suggested diamond formation at pressure as low as 10–20 GPa (at 2000–3000 K), whereas the *ab initio* simulations [132] found dissociation of methane, but synthesis of short alkane-chains at ~ 100 GPa and diamond at pressures not lower than 300 GPa (note that simulations were carried out at 4000–5000 K).

The present work allows us to make a rough estimate of the conditions that are necessary to yield appreciable diamond nucleation on astronomical timescales.

In this context, it is crucial to note that neither carbon stars nor carbon-rich planets consist of pure carbon. In practice, the carbon concentration may be as high as $\sim 50\%$ in carbon-rich stars [127, 128], but much less (1–2% [129, 96, 133, 130]) in Uranus and Neptune. To give a reference point, it is useful to estimate an upper bound to the diamond nucleation rate by considering the rate at which diamonds would form in a hypothetical environment of pure, metastable liquid carbon. To this end we use our numerical data on the chemical potential of liquid carbon and diamond and our numerical estimate of the diamond-liquid surface free energy, to estimate the nucleation barrier of diamond as a function of temperature and pressure. We then use CNT to estimate the rate of diamond nucleation.

To do so, we need to extend the estimate of the nucleation rate from the triple point pressure (around 16 GPa) up to 100 GPa, and from the melting temperatures ($T_m^A = 6600$ K and $T_m^B = 5000$ K, respectively) to 35 % under-cooling (at which diffusion in our sample becomes negligible on the - far from astronomical - time-scales of our simulations). To make such an

extrapolation, we make use of Eqn.’s 10, 9, and 11. The state-point dependent quantities are the solid and liquid number densities ρ_L and ρ_S , the self-diffusion coefficient D , the surface free energy γ , the difference in chemical potential between the liquid and the solid $\Delta\mu$, and the critical cluster size n^* . We estimate them in the following way: the densities are directly measured by Monte Carlo simulations of the solid and the liquid; the self diffusion coefficient is extrapolated assuming an Arrhenius behaviour of the metastable liquid (see Appendix B); the chemical potential difference is interpolated via Eq. 12 between 30 and 85 GPa. $\Delta\mu$ then also follows by linear interpolation. Concerning the surface free-energy, we assume that $\gamma(P, T)$ linearly depends on c_4 , the equilibrium concentration of 4-fold coordinated atoms at the selected state point. This quantity is easily measured in the Monte Carlo simulations. The nucleation barrier height is given by Eq. 9, where the geometrical factor c is the same for all cluster sizes. It is obvious that we have to make rather drastic assumptions in order to estimate the nucleation rate in the experimentally relevant regime. We believe that our assumptions are reasonable, but one should not expect the resulting numbers to provide more than a rough indication.

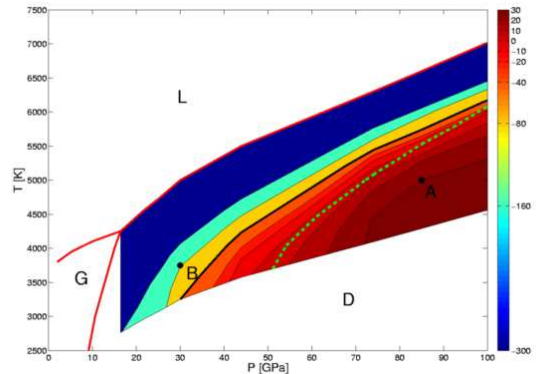


Figure 15: The figure shows part of the carbon phase diagram from Ref. [134] and the iso-nucleation rate zones. The solid red curves represent the coexistence curves from Ref. [134]. $P_A = 85$ GPa, $T_A = 5000$ K and $P_B = 30$ GPa, $T_B = 3750$ K. Along the green dashed curve the ratio of 3-fold and 4-fold coordination in the liquid is 1:1. The numbers on the right indicate the base 10 logarithm (or the order of magnitude) of the crystal nucleation rate from molten carbon (in $m^{-3}s^{-1}$). The continuous black curve is the boundary of the region above which nucleation rate becomes negligible ($< 10^{-40} m^{-3}s^{-1}$).

Figure 15 shows that there is a region of some 1000K below the freezing curve (continuous red curve) where diamond nucleation is less than $10^{-40} \text{ m}^{-3} \text{ s}^{-1}$ (above the continuous black line). If the rate is lower than this number, not a single diamond could have nucleated in a Uranus-sized body during the life of the universe. As can be seen from the figure, our simulations for state point B are outside the regime where observable nucleation would be expected. Note that this latter conclusion is not based on any extrapolation.

As mentioned above, carbon stars and planets do not consist of pure carbon. Hence, we have to consider the effect of dilution on the crystallization process. To do so, we make a very “conservative” assumption, namely that nucleation takes place from an ideal mixture of C, N, O and H [135]. If this were not the case, then either demixing would occur, in which case we are back to the previous case, or the chemical potential of carbon in the liquid is lower than that in pure carbon, which would imply that the thermodynamic driving force for diamond crystallization is less than in pure liquid carbon. In Fig. 16, we show how dilution affects the regime where diamond nucleation is possible. To simplify this figure, we do not vary pressure and temperature independently but assume that they follow the adiabatic relation that is supposed to hold along the isentrope of Uranus [136] and we use the ideal-mixture expression for the chemical potential $\beta\Delta\mu = \beta\Delta\mu_0 + \beta\ln([C])$, where $\beta\Delta\mu_0$ is the chemical potential difference between the solid and the liquid for the pure substance (C) and $[C]$ is the concentration of carbon in the fluid mixture.

Not surprisingly, Fig. 16 shows that dilution of the liquid decreases the driving force for crystallization. In fact, no stable diamond phase is expected for carbon concentrations below 8%. Moreover, there is a wide range of conditions where diamonds could form in principle, but never will in practice. Assuming that, for a given pressure, the width of this region is the same as in the pure C case (almost certainly a serious underestimate), we arrive at the estimate in Fig. 16 of the region where nucleation is negligible (i.e. less than one diamond per planet per life-of-the-universe). From this figure, we see that quite high carbon concentrations (over 15%) are needed to get homogeneous diamond nucleation. Such conditions do exist in white dwarfs, but certainly not in Uranus or Neptune.

Appendix A: LCBOP II

In this appendix, we describe the main features of the latest addition to the LCBOP family. This potential has been used in Ref. [40, 54, 137]. However, the sim-

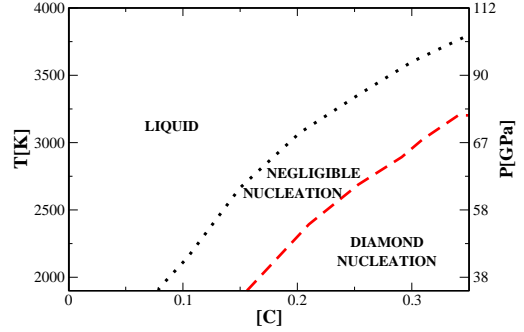


Figure 16: Diamond nucleation boundary as a function of carbon concentration: in the plot, the rate is zero (no thermodynamic driving force to nucleation) in the top region (liquid), it is negligible ($< 10^{-40} \text{ m}^{-3} \text{ s}^{-1}$) in the middle region and non-negligible ($> 10^{-40} \text{ m}^{-3} \text{ s}^{-1}$) in the bottom-right region. We call the nucleation rate negligible if it corresponds to less than one cluster per Uranus-sized planet over a period of 10^{10} years. The left hand y-axis represents the temperature; the right-hand y-axis indicates the corresponding pressure for a Uranus-like isentrope (see Ref. [129, 96, 133, 130]).

ulations discussed in the present paper are based on LCBOP I⁺.

Middle range interactions. Although LCBOP I⁺ gave an improved description of most liquid phase properties, like coordination distributions as a function of density, as compared to the bond-order potentials without LR interactions (Brenner, CBOP[138]), the radial distribution function showed a too marked minimum after the first shell of neighbors, as compared to ab-initio calculations (see Fig. 23). This deficiency was attributed to the relatively short cut-off of 2.2 \AA for the SR interactions, giving rise to a spurious barrier for bond formation around 2.1 \AA . Therefore, for LCBOP II, the total binding energy expression was extended with so-called MR interactions as:

$$E_b = \frac{1}{2} \sum_{i,j}^{N_{at}} \left(S_{ij}^{sr} V_{ij}^{sr} + (1 - S_{ij}^{sr}) V_{ij}^{lr} + \frac{1}{\sqrt{Z_i^{mr}}} S_{ij}^{mr} V_{ij}^{mr} \right) \quad (20)$$

The first two terms on the right-hand side represent the SR and LR interactions respectively, where S_{ij}^{sr} smoothly switches between both interactions within the interval $1.7 \text{ \AA} \leq r_{ij} \leq 2.2 \text{ \AA}$, with $S^{sr}(1.7) = 1$ and $S^{sr}(2.2) = 0$. The last term represents the MR interactions, where V_{ij}^{mr} is a purely attractive potential and Z_i^{mr} is a sort of MR coordination number defined

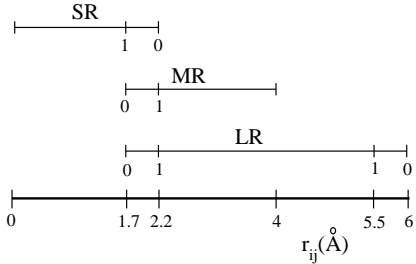


Figure 17: Schematic representation of the domains of the three types of interactions. The numbers 0 and 1 below the lines indicate the values of the switch functions as well as the intervals where these switch functions are applied. As an example, the SR interactions is smoothly switched off between $r_{ij} = 1.7 \text{ \AA}$ and $r_{ij} = 2.2 \text{ \AA}$.

as:

$$Z_i^{mr} = \frac{\left(\sum_j S_{ij}^{mr} V_{ij}^{mr}\right)^2}{\sum_j \left(S_{ij}^{mr} V_{ij}^{mr}\right)^2} \quad (21)$$

to account for many body effects. The switch function $S_{ij}^{mr} = S^{mr}(r_{ij})$, going from 0 to 1 between $r_{ij} = 1.7 \text{ \AA}$ and $r_{ij} = 2.2 \text{ \AA}$, smoothly excludes the MR interactions for distances smaller than 1.7 \AA . For clarity, the ranges of the various interactions in Eq. 20 are schematically represented in Fig. 17. The MR interaction was fitted to ab-initio calculations of single, double and triple bond dissociation curves. For the single bond, the tail of the interaction vanishes beyond 4 \AA . V_{ij}^{mr} is the product of a simple polynomial $V_{P,ij}^{mr}$ with a smooth cut-off at 4 \AA and an environment dependent switch function $S_{\theta}^{mr}(\{\theta_{ijk}\})$, depending on the angles between $\mathbf{r}_{ij} = \mathbf{r}_j - \mathbf{r}_i$ and $\mathbf{r}_{ik} = \mathbf{r}_k - \mathbf{r}_i$ ($\forall k \neq j$), where atom k is a SR neighbour of atom i , i.e. $|\mathbf{r}_{ik}| < 2.2$. Thus, while the MR interactions give an extension of the covalent interactions beyond the SR cut-off distance 2.2 \AA in situations where this is appropriate, its environment dependence relies only on the SR nearest neighbours (within 2.2 \AA), a quite convenient property for the sake of efficiency. The switch S_{θ}^{mr} acts in such a way that V_{ij}^{mr} is only non-zero when the angles θ_{ijk} are relatively large. This is illustrated schematically in Fig. 18. In particular, the definition of $S_{\theta,ij}^{mr}$ makes V_{ij}^{mr} vanish for any pair ij in all bulk crystal structures. So the addition of the MR interactions does not require reparametrization of the SR and LR potential terms.

The reactivity of atoms depends on whether these atoms are well surrounded by neighbours or not. Typically, an atom with a dangling bond wants to make another bond. To include this effect, the MR poten-

tial is made dependent on the so-called dangling bond number N_i^{db} , i.e. $V_{P,ij}^{mr} = V_{P,ij}^{mr}(N_i^{db})$. For an atom with $N_i^{db} = 1$, the MR interaction is stronger than for an atom with $N_i^{db} = 0$.

Extended coordination dependence of angular function. For LCBOP2 the correction of the angle dependent part of the bond order for configurations involving low coordinations and small angles has been further extended, involving a gradual coordination dependence of the angular term over a wide range of coordinations.

Anti-bonding. Another new feature of LCBOP2 is the addition of an anti-bonding correction to the bond order. An example of a situation where one electron remains unpaired in a non-bonding state is depicted in Fig. 19(b). Clearly, this situation is unfavourable as compared to the situation in Fig. 19(c). This effect cannot be captured in the conjugation term and has therefore been included as a separate, anti-bonding term.

Torsion. As it has been clearly demonstrated in Ref. [45], the torsion interaction for a bond ij between an atom i and an atom j is strongly dependent on conjugation, i.e. on the coordinations of the neighbours $k(\neq j)$ of i and $l(\neq i)$ of j . This was already partly included in LCBOP1+. However, for LCBOP2, the conjugation dependence of the torsion interactions was fully extended and fitted to ab-initio calculations of the torsion barrier for all the possible conjugation situations.

In addition to that, LCBOP2 includes a redefinition of the torsion angle, in order to avoid the 'spurious' torsion that occurs using the traditional definition.

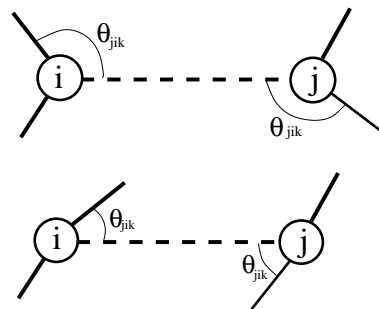


Figure 18: Example of a typical situations where MR interactions are active (upper graph) and where they are switched off by the switch function S_{θ} (lower graph), since S_{θ} vanishes for small bond angles θ_{jik} and θ_{ijl} .

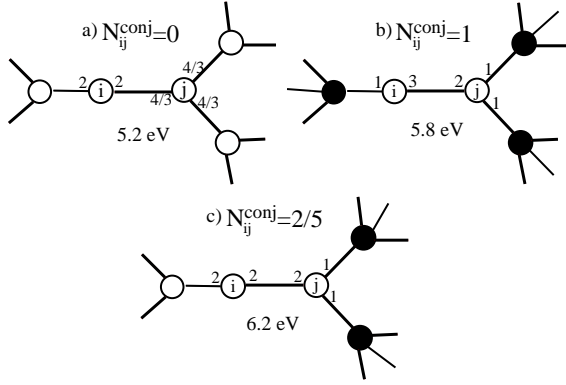


Figure 19: Illustration of configurations where the bond energy is not monotonously dependent on N_{ij}^{conj} , due to the fact that bonding is less effective when the electron supply from atom i , N_{ij}^{el} , is not equal to that from atom j , N_{ji}^{el} . A correct description of each of the three cases was achieved by adding a negative anti-bonding term to the bond order which depends on $\Delta N_{ij}^{el} = N_{ij}^{el} - N_{ji}^{el}$. The resulting binding energy is given below each configuration (see Fig. 20).

Traditionally, the torsion angle ω_{ijkl} is defined as:

$$\cos(\omega_{ijkl}) = \frac{\mathbf{t}_{ijk} \cdot \mathbf{t}_{ijl}}{|\mathbf{t}_{ijk}| |\mathbf{t}_{ijl}|} = \frac{(\mathbf{r}_{ij} \times \mathbf{r}_{ik}) \cdot (\mathbf{r}_{ij} \times \mathbf{r}_{jl})}{|\mathbf{r}_{ij} \times \mathbf{r}_{ik}| |\mathbf{r}_{ij} \times \mathbf{r}_{jl}|} \quad (22)$$

which, assuming torsion to be non-vanishing only between sp^2 bonded atoms i and j , gives rise to four torsion contributions to the bond order. With the definition of Eq. 22, both situations depicted in Fig. 21b and c give rise to a non-zero torsion angle. However, in both situations there is actually no torsional distortion but only a bending distortion, which is already taken into account by the angular term in the bond order. Thus, one would like to have $\omega_{ijkl} = 0$ for the cases in Fig. 21b and c, in disagreement with the most right-hand side expression in Eq. 22. Another problem of expression 22 is that it has a singularity for configurations where \mathbf{r}_{ij} is parallel to \mathbf{r}_{ik} (or \mathbf{r}_{il}). For the liquid phase at high temperature such situation are easily accessible.

For LCBOPH, the problem of 'spurious' torsion has been tackled by a redefinition of the vectors \mathbf{t}_{ijk} in Eq. 22, reading:

$$\begin{aligned} \mathbf{t}_{ijk} = & \hat{\mathbf{r}}_{ij} \times (\hat{\mathbf{r}}_{ik_1} - \hat{\mathbf{r}}_{ik_2}) + \\ & + \frac{\sqrt{3}}{2} (\hat{\mathbf{r}}_{ij} \cdot (\hat{\mathbf{r}}_{ik_1} - \hat{\mathbf{r}}_{ik_2})) (\hat{\mathbf{r}}_{ij} \times (\hat{\mathbf{r}}_{ik_1} + \hat{\mathbf{r}}_{ik_2})) \end{aligned} \quad (23)$$

and likewise for \mathbf{t}_{jil} . Inserting these vectors into Eq. 22, leading to a different right-hand side, reproduces

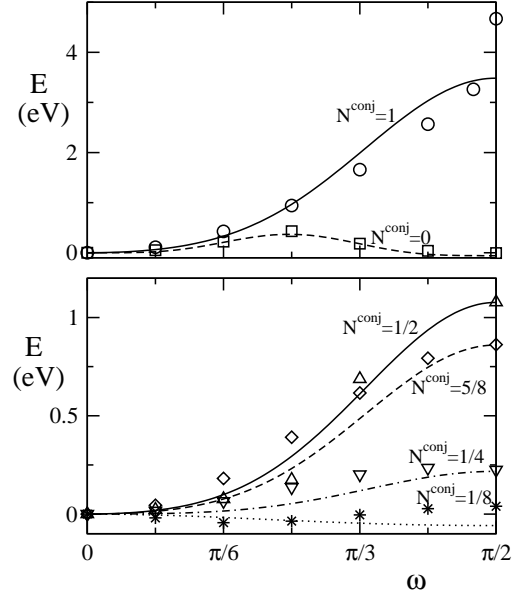


Figure 20: Torsional barriers according to LCBOPH and DF calculations for the six possible values of N_{ij}^{conj} for an ij bond between sp^2 atoms i and j . Symbols represent the DF results, curves the fits obtained by the LCBOPH. Top panel: torsional barriers for the extreme values of N_{ij}^{conj} , related to the conjugated ($N_{ij}^{conj}=0$, squares and dashed curve) and double bonds ($N_{ij}^{conj}=1$, circles and solid curve). Bottom panel: intermediate values of N_{ij}^{conj} : 1/8 (stars and dotted curve), 1/4 (down triangles and dashed-dotted curve), 1/2 (up triangles and solid curve) and 5/8 (diamonds and dashed curve). Note the complex behaviour of the curves for the values 1/2 and 5/8, where the barrier at $\pi/2$ is higher for $N_{ij}^{conj}=1/2$ than for $N_{ij}^{conj}=5/8$. The top panel alone applies also to LCBOPH+ (see Appendix A in [40] for details.)

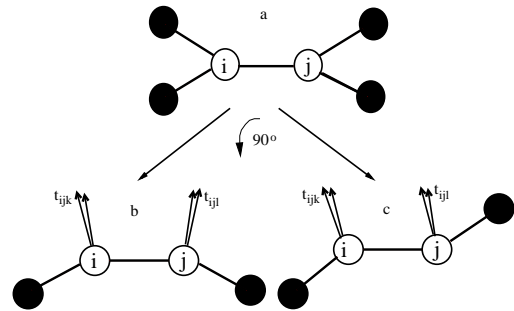


Figure 21: Illustration of the occurrence of spurious torsion when using the definition of Eq. 22 (most right-hand side) for the torsion angles.

the same ω_{ijkl} as the traditional definition for any torsional distortion without bending and yields $\omega_{ijkl} = 0$ for both situations depicted in Fig. 21, as it should be. In addition, it gives a good interpolation for any other configuration, and it has no singularities. Note that for the two distortions depicted in Fig. 21, the second term in Eq. 24 vanishes, and the vectors \mathbf{t}_{ijk} and \mathbf{t}_{jil} are parallel, implying indeed $\omega_{ijkl} = 0$.

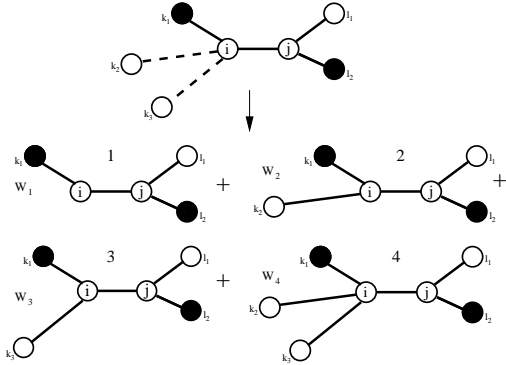


Figure 22: For LCBOP2, a fractional coordination situation is treated as a weighted superpositions of integer coordination situations, as illustrated in this picture. Dashed lines indicate partial bonds, solid lines are for full bonds.

Interpolation for fractional coordinations. The conjugation term $F_{ij}^{conj}(N_{ij}, N_{ji}, N_{ij}^{conj})$ for a bond ij depends on the reduced coordinations N_{ij} and N_{ji} of the atoms i and j , and on the conjugation number N_{ij}^{conj} . The reduced coordination N_{ij} is defined as:

$$N_{ij} = \sum_{k \neq i, j} S_Z(r_{ik}) \quad (24)$$

and likewise for N_{ji} , where $S_Z(r_{ik})$ is a switch function for the coordination, smoothly going from 1 to 0 for r_{ik} going from 1.7 Å and 2.2 Å. F_{ij}^{conj} is fitted to integer coordination configurations with only full neighbours, i.e. with $S_Z(r_{ik}) = S_Z(r_{jl}) = 1 \forall k, l$. This poses the problem of how to determine F_{ij}^{conj} for configurations with fractional bonds, i.e. configurations with $S_Z(r_{ik}) < 1$ for one or more neighbours k . David Brenner, the inventor of the conjugation term, proposed to use a 3D spline [52]. However, since the values on the integer argument nodes are rather scattered, a spline unavoidably introduces unphysical oscillations. For LCBOP2, we found an alternative solution to this problem which is schematically illustrated in Fig. 22. In this approach, the conjugation term for configurations with fractional coordination is defined as a weighted superposition of conjugation terms for

configurations with integer configurations, the weight factors W_c for the configuration $c (= 1, \dots, 4)$ being defined in terms of the switch functions $S_Z(r_{ik})$. For instance, for the situation in Fig. 22, the conjugation term is given by:

$$\begin{aligned} F_{ij}^{conj} &= (1 - S_{Z,ik_2})(1 - S_{Z,ik_3})F_{ij}^{conj}(1, 2, N_{ij,1}^{conj}) + \\ &+ S_{Z,ik_2}(1 - S_{Z,ik_3})F_{ij}^{conj}(2, 2, N_{ij,2}^{conj}) + \\ &+ (1 - S_{Z,ik_2})S_{Z,ik_3}F_{ij}^{conj}(2, 2, N_{ij,3}^{conj}) + \\ &+ S_{Z,ik_2}S_{Z,ik_3}F_{ij}^{conj}(3, 2, N_{ij,4}^{conj}) \end{aligned}$$

where $N_{ij,c}^{conj}$ are the conjugation numbers for the four configurations in Fig. 22.

Results with LCBOP2. LCBOP2 proved to be more accurate than its predecessors in describing defects and surfaces of the solid phases [40]. In the liquid phases the improvement of LCBOP2 is immediately evident when looking at radial distribution functions at different densities (Fig. 23). The main discrepancy between LCBOP1+ and the reference data from DF-MD calculations [46, 54] was found at the first minimum, at around 2 Å. LCBOP1+ predicted a much deeper minimum than DF-MD. This discrepancy is completely eliminated by LCBOP2. We also know that the melting line of diamond predicted by LCBOP2 is about 500 K lower than for LCBOP1+ at ~ 60 GPa [54], more consistently with ab-initio predictions of the diamond melting line [105, 106]. In [54] we also thoroughly analyzed the properties of the liquid. Interestingly, by extrapolating the equations of state of the liquid at temperatures at which our relatively small samples actually froze, we found that a critical point for the graphite-like into diamond-like transition is present at 1230 K. The precise value might be inaccurate, since it is found far outside the sampled region, still the shapes of the higher temperature equations of state point towards the existence of such critical isotherm. As is the case for the much speculated water LLPT [29, 30] an unreachable critical point might still be responsible of some peculiar behaviour of the system at higher temperatures, such as the enormous change in nucleation rate with pressure.

Appendix B: Self-diffusion coefficient

When computing the kinetic pre-factor to get the nucleation rate, we have to consider the fact that for our model potential, LCBOP1+, only a Monte Carlo code is available. In order to evaluate the self-diffusion coefficient needed to compute the CNT kinetic pre-factor, we infer the scaling factor between the Monte Carlo “time-step” and the MD time-step [139] by propagating a 128 carbon atoms system via Car-Parrinello

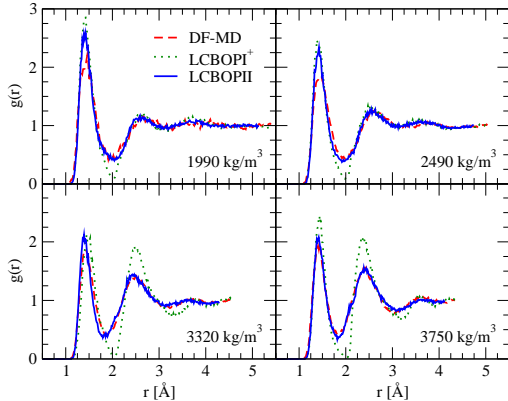


Figure 23: Comparison of the radial distribution functions at 6000 K and four selected densities between LCBOPH, LCBOPH+, and the reference data taken from our own DF-MD simulations.

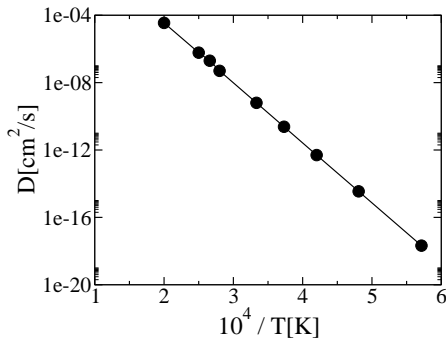


Figure 24: Arrhenius plot for the super-cooled liquid carbon. The activation energy is $E_A = 7\text{eV}$ from Ref.[141].

Molecular Dynamics CPMD code [140] starting from a configuration equilibrated with LCBOPH+. Note the reasonably good agreement between the *static* properties of the liquid carbon computed with LCBOPH+ and the same computed by means of CPMD (with the BP functional) [46, 54]. Data for the high pressure state point come from simulations used in Ref. [46], whereas data for the low pressure state point come from a new simulation where the time rescaling is state-point dependent, obtained with the same technical details as reported in [46].

We use the fact that molten carbon is an Arrhenius-like liquid: therefore, once the activation energy is known, we compute the viscosity as a function of temperature and by means of the Stokes-Einstein relation obtain the diffusion coefficient. In the nineteen-fifties, Kanter [141] estimated the relevant activation energy of liquid carbon to be $E_A = 683 \frac{\text{kJ}}{\text{mol}}$. Subsequently,

Fedosayev [142] reported a measurement of the molten carbon viscosity: $\eta = 5 \times 10^{11}$ poise at $T = 1860\text{K}$. We estimate the self-diffusion coefficient at the same temperature by means of the Stokes-Einstein relation [143]

$$D = \frac{k_B T}{\eta a}, \quad (25)$$

where $a = 1.54\text{Å}$ and k_B is the Boltzmann's constant: $D(1860\text{K}) = 3.3 \times 10^{-17} \text{cm}^2/\text{s}$. Since molten carbon is an Arrhenius-like fluid [144],

$$D(T) = D_0 \exp\left(-\frac{E_A}{k_B T}\right), \quad (26)$$

we obtain D_0 : $D_0 = 470\text{cm}^2/\text{s}$, and then extrapolate the diffusion coefficient for different temperatures, as shown in Fig. 24 and Table 3.

T[K]	D[Å²/s]	T[K]	D[Å²/s]
1750	2.1×10^{-2}	3000	6.3×10^6
2080	3.5×10^1	3300	7.6×10^7
2380	5.0×10^4	3570	5.0×10^8
2680	2.4×10^5	3760	2.0×10^9

Table 3: Self diffusion coefficient as a function of temperature.

We then find that at state point *A*, $D_A = 3.5 \times 10^{-5} \text{cm}^2/\text{s}$, whereas at state point *B*, $D_B = 2 \times 10^{-7} \text{cm}^2/\text{s}$.

We also use a Car-Parrinello Molecular Dynamics [140] to calculate the self-diffusion coefficient by means of the mean square displacement: at state point *A* $D = 2.3 \times 10^{-5} \text{cm}^2/\text{s}$, which matches surprisingly well with the diffusion coefficient estimated by means of the Arrhenius law, $D = 3.5 \times 10^{-5} \text{cm}^2/\text{s}$.

Acknowledgments

The work of the FOM Institute is part of the research program of FOM and is made possible by financial support from the Netherlands Organization for Scientific Research (NWO). We gratefully acknowledge financial support from NWO-RFBR Grant No 047.016.001 and FOM grant 01PR2070. We acknowledge support from the Stichting Nationale Computerfaciliteiten (NCF) and the Nederlandse Organisatie voor Wetenschappelijk Onderzoek (NWO) for the use of supercomputer facilities. LMG wishes to thank his wife, Sara Iacopini, for helping him in scanning and summarizing the literature mentioned in section 3.1.

References

- [1] A. G. WHITTAKER, *Science* **200**, 4343 (1978).

- [2] P. P. K. SMITH and P. R. BUSECK, *Science* **216**, 984 (1982).
- [3] H. W. KROTO, J. R. HEATH, S. C. O'BRIEN, R. F. CURL, and R. E. SMALLEY, *Nature* **318**, 162 (1985).
- [4] S. IJIMA, *Nature* **354**, 56 (1991).
- [5] K. NOVOSELOV, A. K. GEIM, S. V. MOROZOV, D. JIANG, Y. ZHANG, S. V. DUBONOS, I. V. GRIGORIEVA, and A. A. FIRSOV, *Science* **306**, 666 (2004).
- [6] A. JAYARAMAN, R. C. NEWTON, and J. M. McDONOUGH, *Phys. Rev.* **159**, 527 (1967).
- [7] R. BELLISSANT, C. BERGMAN, R. CEOLIN, and J. P. GASPARD, *Phys. Rev. Lett.* **59**, 661 (1987).
- [8] D. A. YOUNG, *Phase Diagrams of the Elements*, University of California Press, Berkeley, 1991.
- [9] O. OHTAKA, H. ARIMA, H. FUKUI, W. UTSUMI, Y. KATAYAMA, and A. YOSHIASA, *Phys. Rev. Lett.* **92**, 155506 (2004).
- [10] D. ISHIKAWA, M. INUI, K. MATSUDA, K. TAMURA, S. TSUTSUI, and A. Q. R. BARON, *Phys. Rev. Lett.* **93**, 097801 (2004).
- [11] V. V. BRAZHKNIN, R. N. VOLOSHIN, S. V. POPOVA, and A. G. UMNNOV, *Phys. Lett. A* **154**, 413 (1991).
- [12] A. G. UMNNOV and V. V. BRAZHKNIN, *High Pressure Research* **13**, 233 (1995).
- [13] V. V. BRAZHKNIN, R. N. VOLOSHIN, and S. V. POPOVA, *Pis'ma v ZhETF* **50**, 424 (1989), English translation in : *JETP Letters* **50**, 424 (1989).
- [14] C. A. ANGELL, S. BORICK, and M. GRABOW, *J. of Non-cryst. Solids* **205**, 463 (1996).
- [15] P. BEAUCAGE and N. MOUSSEAU, *J. Phys.: Condens. Matter* **17**, 2269 (2005).
- [16] A. G. UMNNOV and V. V. BRAZHKNIN, *High Temp. - High Pressure* **25**, 221 (1993).
- [17] S. T. WEIR, A. C. MITCHELL, and W. J. NELLIS, *Phys. Rev. Lett.* **76**, 1860 (1996).
- [18] V. V. BRAZHKNIN, R. N. VOLOSHIN, S. V. POPOVA, and A. G. UMNNOV, *High Pressure Research* **6**, 363 (1992).
- [19] M. ROSS and F. ROGERS, *Phys. Rev. B* **74**, 024103 (2006).
- [20] G. D. MUKHERJEE and R. BOEHLER, *Phys. Rev. Lett.* **99**, 225701 (2007).
- [21] L. PAULING and M. SIMONETTA, *J. Chem. Phys.* **20**, 29 (1952).
- [22] D. HOHL and R. O. JONES, *Phys. Rev. B* **50**, 17047 (1994).
- [23] Y. KATAYAMA, T. MIZUTANI, W. UTSUMI, O. SHIMOMURA, M. YAMAKATA, and K. FUNAKOSHI, *Nature* **403**, 170 (2000).
- [24] G. MONACO, S. FALCONI, W. A. CRICHTON, and M. MEZOUAR, *Phys. Rev. Lett.* **90**, 255701 (2003).
- [25] T. MORISHITA, *Phys. Rev. Lett.* **87**, 105701 (2001).
- [26] Y. SENDA, F. SHIMOJO, and K. OSHINO, *J. Phys.: Condens. Matter* **14**, 3715 (2002).
- [27] L. M. GHIRINGHELLI and E. J. MEIJER, *J. Chem. Phys.* **122**, 184510 (2005).
- [28] L. M. GHIRINGHELLI and E. J. MEIJER, *J. Phys.: Condens. Matter* **19**, 416104 (2007).
- [29] O. MISHIMA and H. E. STANLEY, *Nature* **396**, 329 (1998).
- [30] G. FRANZESE, G. MALESCIO, A. SKIBINSKY, S. BULDYREV, and H. STANLEY, *Nature* **409**, 692 (2001).
- [31] P. H. POOLE, M. HEMMATI, and C. A. ANGELL, *Phys. Rev. Lett.* **79**, 2281 (1997).
- [32] J. P. IITIE, *Phys. Rev. Lett.* **63**, 398 (1989).
- [33] E. RAPOPORT, *J. Chem. Phys.* **46**, 2891 (1967).
- [34] S. STRÄSSLER and C. KITTEL, *Phys. Rev.* **139**, A758 (1965).
- [35] I. L. APTEKAR and E. G. PONYATOVSKY, *Phys. Met. Metallogr.* **25**, 10 (1968).
- [36] I. A. KORSUNSKAYA, D. S. KAMENETSKAYA, and I. L. APTEKAR, *Fiz. metal. metalloved.* **34**, 942 (1972), English version in: *Phys. Met. Metallogr. (USSR)* **34**, 39 (1972).
- [37] V. V. BRAZHKNIN, S. V. POPOVA, and R. N. VOLOSHIN, *High Pressure Research* **15**, 267 (1997).
- [38] H. TANAKA, *Phys. Rev. E* **62**, 6968 (2000).
- [39] J. H. LOS and A. FASOLINO, *Phys. Rev. B* **68**, 024107 (2003).
- [40] J. H. LOS, L. M. GHIRINGHELLI, E. J. MEIJER, and A. FASOLINO, *Phys. Rev. B* **72**, 214102 (2005), Erratum: *Phys. Rev. B* **73**, 229901(E) (2006).
- [41] L. M. GHIRINGHELLI, C. VALERIANI, E. J. MEIJER, and D. FRENKEL, *Phys. Rev. Lett.* **99**, 055702 (2007).
- [42] S. B. SINNOTT, O. A. SHENDEROVA, C. T. WHITE, and D. W. BRENNER, *Carbon* **36**, 1 (1998).
- [43] A. PETUKHOV and A. FASOLINO, in *Technical Proceedings of the ICCN 2001 Int. Conf. on Computational Nanoscience*, Applied Computational Research Society, also at www.cr.org/publications/ICCN2001/.
- [44] S. STUART, A. TUTEIN, and J. HARRISON, *J. Chem. Phys.* **112**, 6472 (2000).
- [45] C. J. WU, J. N. GLOSLI, G. GALLI, and F. H. REE, *Phys. Rev. Lett.* **89**, 135701 (2002).
- [46] L. M. GHIRINGHELLI, J. H. LOS, E. J. MEIJER, A. FASOLINO, and D. FRENKEL, *Phys. Rev. B* **69**, 100101(R) (2004).
- [47] P. W. ANDERSON, *Phys. Rev. Lett.* **21**, 13 (1968).
- [48] P. W. ANDERSON, *Phys. Rev.* **181**, 25 (1969).

- [49] J. D. WEEKS and P. W. ANDERSON, *J. Chem. Phys.* **58**, 1388 (1973).
- [50] G. C. ABELL, *Phys. Rev. B* **31**, 6184 (1985).
- [51] J. TERSOFF, *Phys. Rev. Lett.* **61**, 2879 (1988).
- [52] D. W. BRENNER, *Phys. Rev. B* **42**, 9458 (1990), Erratum: *Phys. Rev. B* **46**, 1948 (1992).
- [53] D. W. BRENNER, O. A. SHENDEROVA, J. A. HARRISON, S. J. STUART, B. NI, and S. B. SINNOTT, *J. Phys.: Condens. Matter* **14**, 783 (2002).
- [54] L. M. GHIRINGHELLI, J. H. LOS, A. FASOLINO, and E. J. MEIJER, *Phys. Rev. B* **72**, 214103 (2005).
- [55] L. M. GHIRINGHELLI, *On the Nature of phase transitions in covalent liquids*, PhD thesis, 2006, It can be downloaded from: <http://dare.uva.nl/document/18341>.
- [56] H. W. B. ROOZEBOOM, *Die heterogenen Gleichgewichte, Braunschweig*, volume 1, 1901.
- [57] G. TAMMAN, *Zeit. Phys. Chem* **69** (1909).
- [58] F. D. ROSSINI and R. S. JESSUP, *J. Res. Nat'l. Bur. Stds.* **21**, 491 (1938).
- [59] O. I. LEIPUNSKII, *Uspekhi Khim.* **8**, 1519 (1939).
- [60] M. J. BASSET, *J. Chem. Radium* **10**, 217 (1939).
- [61] P. W. BRIDGMAN, *J. Chem. Phys.* **15**, 92 (1947).
- [62] R. LILJEBLAD, *Arkiv Kemi* **8**, 423 (1955).
- [63] R. BERMAN and F. SIMON, *Z. Elektrochem.* **59**, 333 (1955).
- [64] F. P. BUNDY, H. T. HALL, H. M. STRONG, and R. H. WENTORF, *Nature* **176**, 51 (1955).
- [65] F. P. BUNDY, *J. Chem. Phys.* **38**, 618 (1963).
- [66] I. I. ALTHERTUM, W. FEHSE, and M. PIRANI, *Z. Elektrochem.* **31**, 313 (1925).
- [67] G. J. SCHOESSOW, *Phys. Rev. Lett.* **21**, 11 (1968).
- [68] J. HEREMANS, C. H. OLK, G. L. EESLEY, J. STEINBECK, and G. DRESSELHAUS, *Phys. Rev. Lett.* **60**, 5 (1988).
- [69] A. G. WHITTAKER and P. L. KINTNER, Carbon vapor pressure in the range 3450 to 4500 K and evidence for melting at ~ 3800 K, in *Abstract of the 12th biennial conf. on carbon*, Pittsburgh, Pa., 1975.
- [70] J. W. SHANER, J. M. BROWN, A. C. SWENSON, and R. G. MCQUEEN, *J. Phys.* **45**, 235 (1984).
- [71] A. CEZAIIRLIYAN and A. P. MILLER, *Int. J. Thermophys.* **11**, 643 (1990).
- [72] G. POTTLAGHER, R. S. HIXSON, R. S. MELNITZKY, E. KASCHNITZ, M. A. WINKLER, and H. JAGER, *Thermochim. Acta* **218**, 183 (1993).
- [73] F. P. BUNDY, W. A. BASSETT, M. S. WEATHERS, R. J. HEMLEY, H. K. MAO, and A. F. GONCHAROV, *Carbon* **34**, 141 (1996).
- [74] M. TOGAYA, *Phys. Rev. Lett.* **79**, 2474 (1997).
- [75] M. MUSELLA, C. RONCHI, M. BRYKIN, and M. SHEINDIN, *J. Appl. Phys.* **84**, 2530 (1998).
- [76] E. I. ASINOVSKII, A. V. KIRILLIN, and A. V. KOSTANOVSKII, *High Temperature* **35**, 704 (1997).
- [77] E. I. ASINOVSKII, A. V. KIRILLIN, A. V. KOSTANOVSKII, and V. E. FORTOV, *High Temperature* **36**, 716 (1998).
- [78] P. S. DECARLI and J. C. JAMIESON, *Science* **133**, 1821 (1961).
- [79] B. J. ALDER and R. H. CHRISTIAN, *Phys. Rev. Lett.* **7**, 367 (1961).
- [80] F. P. BUNDY, *J. Chem. Phys.* **38**, 631 (1963).
- [81] J. C. JAMIESON, *Science* **161**, 363 (1963).
- [82] F. P. BUNDY, *Physical Chemistry* (1969), Bakhuis Roozeboom award lecture, 25-10-1969.
- [83] J. A. VAN VECHTEN, *Phys. Rev. B* **7**, 1479 (1973).
- [84] R. GROVER, *J. Chem. Phys.* **71**, 3824 (1979).
- [85] A. E. GORESY and G. DONNAY, *Science* **161**, 363 (1968).
- [86] T. VENKATESAN, D. C. JACOBSON, J. M. GIBSON, B. S. ELMAN, G. BRAUNSTEIN, M. S. DRESSELHAUS, and G. DRESSELHAUS, *Phys. Rev. Lett.* **53**, 360 (1984).
- [87] P. HOHENBERG and W. KOHN, *Phys. Rev.* **136**, B864 (1964).
- [88] W. KOHN and L. J. SHAM, *Phys. Rev. A* **140**, 1133 (1965).
- [89] M. T. YIN and M. L. COHEN, *Phys. Rev. Lett.* **50**, 2006 (1983).
- [90] M. T. YIN, *Phys. Rev. B* **30**, 1773 (1984).
- [91] R. BISWAS, R. M. MARTIN, R. J. NEEDS, and O. H. NIELSEN, *Phys. Rev. B* **35**, 1987 (1987).
- [92] S. FAHY and S. G. LOUIE, *Phys. Rev. B* **36**, 3373 (1987).
- [93] J. W. SHANER, J. M. BROWN, A. C. SWENSON, and R. G. MCQUEEN, *J. Phys. (Paris) Colloq.* **45**, C8 (1984).
- [94] M. TOGAYA, in *Science and Technology of New Diamond*, KTK/TSPC, Tokyo, 1990.
- [95] G. GALLI, R. M. MARTIN, R. CAR, and M. PARINELLO, *Science* **250**, 1547 (1990).
- [96] M. ROSS, *Nature* **292**, 435 (1981).
- [97] M. P. GRUMBACH and R. M. MARTIN, *Phys. Rev. B* **54**, 15730 (1996).
- [98] D. K. BRADLEY, J. H. EGGERT, D. G. HICKS, P. M. CELLIERS, S. J. MOON, R. C. CAUBLE, and G. W. COLLINS, *Phys. Rev. Lett.* **93**, 195506 (2004).
- [99] M. VAN THIEL and F. H. REE, *Phys. Rev. B* **48**, 3591 (1993).

- [100] D. A. KOFKE, *J. Chem. Phys.* **98**, 4149 (1993).
- [101] J. ANWAR, D. FRENKEL, and M. G. NORO, *J. Chem. Phys.* **118**, 728 (2003).
- [102] D. FRENKEL and B. SMIT, *Understanding Molecular simulation*, Academic Press, San Diego, California, 2002.
- [103] J. N. GLOSLI and F. H. REE, *Phys. Rev. Lett.* **82**, 4659 (1999).
- [104] J. N. GLOSLI and F. H. REE, *J. Chem. Phys.* **110**, 441 (1999).
- [105] X. WANG, S. SCANDOLO, and R. CAR, *Phys. Rev. Lett.* **95**, 185701 (2005).
- [106] A. A. CORREA, S. A. BONEV, and G. GALLI, *PNAS* **103**, 1204 (2006).
- [107] S. BRYGOO, E. HENRY, P. LOUBEYRE, J. EGGERT, M. KOENIG, B. LOUPIAS, A. BENUZZI-MEOUNAIX, and M. R. LE GLOAHEC, *Nature Materials* **6**, 274 (2007).
- [108] M. VAN THIEL and F. H. REE, *High Pressure Research* **10**, 607 (1992).
- [109] N. S. FATEEVA and L. F. VERESHCHAGIN, *Pis'ma. Zh. Eksp. Teor. Fiz.* **13**, 157 (1971).
- [110] E. PONYATOVSKY, *J. Phys.: Condens. Matter* **15**, 6123 (2003).
- [111] D. W. BRENNER, J. H. HARRISON, C. T. WHITE, and R. J. COLTON, *Thin Solid Films* **206**, 220 (1991).
- [112] J. R. MORRIS, C. Z. WANG, and K. M. HO, *Phys. Rev. B* **52**, 4138 (1995).
- [113] N. A. MARKS, *J. Phys.: Condens. Matter* **14**, 2901 (2002).
- [114] N. A. MARKS, N. C. COOPER, D. R. MCKENZIE, D. G. MCCULLOCH, P. BATH, and S. P. RUSSO, *Phys. Rev. B* **65**, 075411 (2002).
- [115] K.F.KELTON, *Crystal Nucleation in Liquids and Glasses*, volume 45, Academic Press, Boston.
- [116] P. R. TEN WOLDE, M. J. RUIZ-MONTERO, and D. FRENKEL, *J. Chem. Phys.* **104**, 9932 (1996).
- [117] S. AUER and D. FRENKEL, *Nature* **409**, 1020 (2001).
- [118] C. VALERIANI, E. SANZ, and D. FRENKEL, *J. Chem. Phys.* **122**, 194501 (2005).
- [119] C. VALERIANI, *Numerical studies of nucleation pathways of ordered and disordered phases*, PhD thesis, 2007, It can be downloaded from: <http://dare.uva.nl/record/236014>.
- [120] P. R. TEN WOLDE, *Numerical Study of Pathways for Homogeneous Nucleation*, 1997, Downloadable from: www.amolf.nl/publications/theses/wolde/wolde.html.
- [121] G. M. TORRIE and J. P. VALLEAU, *J. Comp. Phys.* **23**, 187 (1977).
- [122] S. AUER and D. FRENKEL, *Advances in Polymer Sciences* **173**, 149 (2005).
- [123] R. J. ALLEN, P. B. WARREN, and P. R. TEN WOLDE, *Phys. Rev. Lett.* **94**, 018104 (2005).
- [124] R. ALLEN, D. FRENKEL, and P. TEN WOLDE, *J. Chem. Phys.* **124**, 024102 (2006).
- [125] L. M. GHIRINGHELLI, J. H. LOS, E. J. MEIJER, A. FASOLINO, and D. FRENKEL, *J. Phys.: Condens. Matter* **17**, S3619 (2005).
- [126] I. SAIKA-VOIVOD, F. SCIORTINO, and P. H. POOLE, *Phys. Rev. E* **63**, 011202 (2000).
- [127] S. E. HAGGERTY, *Science* **285**, 851 (1999).
- [128] U. A. JORGENSEN, *Nature* **332**, 702 (1988).
- [129] J. I. BERGSTRAHL, E. D. MINER, and M. S. MATTHEWS, *Uranus*, University of Arizona Press, Tucson, 1991.
- [130] M. J. KUCHNER and S. SEAGER, *Astr-phys* **0504214** (2005).
- [131] L. R. BENEDETTI, J. H. NGUYEN, W. A. CALDWELL, H. LIU, M. KRUGER, and R. JEANLOZ, *Nature* **286**, 100 (1999).
- [132] F. ANCILOTTO, G. L. CHIAROTTI, S. SCANDOLO, and E. TOSATTI, *Science* **275**, 1288 (1997).
- [133] S. SCANDOLO, G. CHIAROTTI, and E. TOSATTI, *Physics World* **13**, 31 (2000).
- [134] L. M. GHIRINGHELLI, J. H. LOS, E. J. MEIJER, A. FASOLINO, and D. FRENKEL, *Phys. Rev. Lett.* **94**, 145701 (2005).
- [135] J. L. BARRAT, J. P. HANSEN, and R. MOCHKOVITCH, *Astronomy and Astrophysics* **199**, 15 (1988).
- [136] S. SCANDOLO and R. JEANLOZ, *Am. Sc.* **91**, 516 (2003).
- [137] A. FASOLINO, J. H. LOS, and M. I. KATSNELSON, *Nature Materials* **6**, 858 (2007).
- [138] J. LOS and A. FASOLINO, *Computer Physics Communications* **147**, 178 (2002).
- [139] H. E. A. HUITEMA and J. P. VAN DER EERDEN, *J. Chem. Phys.* **110**, 3267 (1999).
- [140] R. CAR and M. PARRINELLO, *Phys. Rev. Lett.* **55**, 2471 (1985).
- [141] M. A. KANTER, *Phys. Rev.* **107**, 655 (1957).
- [142] D. V. FEDOSAYEV, B. V. DERYAGIN, and I. G. VARASAVSKAJA, *Nauka, Moscow* (1984).
- [143] J. P. HANSEN and I. R. M. DONALD, *Theory of simple liquids*, Academic Press.
- [144] P. G. DEBENEDETTI, *Metastable Liquids*, Princeton University Press, 1996.